Application of a Vortex Lattice Method Solver to an Aircraft Sizing Framework

by

Benjamin Davis

A thesis submitted to the Graduate Faculty of
Auburn University
in partial fulfillment of the
requirements for the Degree of
Master of Science

Auburn, Alabama
August 9, 2025

Keywords: Vortex Lattice Method, Aircraft Design, Flight Dynamics, Potential Flow

Approved by

Imon Chakraborty, Chair, Associate Professor of Aerospace Engineering
Roy Hartfield, Walt and Virginia Woltosz Professor of Aerospace Engineering
Anwar Ahmed, Professor of Aerospace Engineering

Abstract

A Vortex Lattice Method (VLM) solver is developed to estimate the aerodynamic performance of lifting surfaces, while operating within the assumptions of Potential Flow. The VLM solution is found by representing an aircraft configuration's lifting surfaces using a mesh of bound vortices and wake segments enabling the computation of the aerodynamic forces and moments acting on the vehicle. Applying this method, the influence of each panel on every other panel is computed. This process inherently incorporates the influence of each lifting surface on every other lifting surface. To extend the applicability of the method beyond incompressible flow, compressibility corrections were applied.

Before the solver was incorporated into an aircraft sizing framework for the evaluation of forces and moments produced by lifting surfaces while in flight, validation studies were completed. Validation of the VLM solver was performed by initially comparing the output with experimental data to verify the spanwise loading and overall lift prediction were accurate. Next, the VLM model was compared with other state-of-the-art Potential Flow solvers, and it was concluded that the model was producing data with a satisfactory level of accuracy.

The VLM solver was then implemented into the Parametric Energy-based Aircraft Configuration Evaluator (PEACE) aircraft sizing framework to combine the VLM solution with fuselage and two-dimensional airfoil data to determine the full aircraft forces and moments. When the fuselage data was combined with the VLM solution, the method produced precise results for low angles of attack. As predicted from the formulation of the Vortex Lattice Method, the solution began to diverge from viscous solutions as the angle of attack increased.

Acknowledgments

Firstly, I would like to thank my family. I could not have done this without your unconditional support. Thank you to Minden and my father for reviewing my writing, and spending hours with me on the phone. Brayden and Amelia, thank you for being with me through this rough time, you are both brilliant and highly motivated, I know that you will do great things.

I grateful for the support provided by VSDDL, and everyone there. My advisor, Dr. C. made this work possible by providing funding and time to accomplish the project. I would like to thank Dr. Anthony Comer for reviewing my draft and providing valuable feedback. Thank you to Bikash for generating FlightStream validation data. I am extremely grateful to my committee, Dr. Hartfield and Dr. Ahmed for their feedback and guidance in this work. I have greatly enjoyed being your student.

I would like to thank the Auburn University Aerospace Engineering department for providing me with an opportunity rich environment while perusing my degrees. My undergraduate experience was greatly enhanced by the extracurricular activities funded by the department, and as a graduate student I have benefited greatly from the resources at my disposal.

Table of Contents

List of Tables

List of Figures

Chapter 1

Introduction

1.1 Motivation

The modern aviation industry is thriving. In 2017, commercial aircraft moved nearly 35% of all goods around the world by value, with container ships accounting for the vast majority of the remainder [1]. For most of our global population, the efficient, practical method for long-haul distances is to use a commercial airliner. Not only are these aircraft the fastest way to travel long distances (e.g. across oceans, geographically sparse land masses), they have incredibly low specific emissions in comparison to other methods of rapid long-haul transportation [2, 3]. Airlines are thriving; and each year, more aircraft are ordered than have been retired, and this trend is only continuing [4, 5].

Flying cars have always been a science fiction dream, but the feasibility of that concept has proven lackluster due to the expense of maintaining an aircraft and the inherent hazard of untrained operators piloting massive vehicles over population centers. The much more likely progression of technology is that airlines will supplement their long-haul fleets with shorter flights as the operating cost of such vehicles decreases with the natural progression of technology. In the not-too-distant future, Urban Air Mobility (UAM) electronic vertical takeoff and landing (eVTOL) aircraft promises faster, quieter, ferry flights across population centers, bringing the benefits that long-haul flights already give to the hands of the everyday commuter [6–9].

In recent years, the development of lighter weight and more energy dense batteries has led to the rapid rise of the true personal aircraft: unmanned aerial vehicles (UAV). The inherent

advantages of these aircraft being smaller, cheaper, and lighter than any other type of aircraft come from the fact that they are not required to carry a human pilot. A bare minimum UAV can be purchased for less than $20, and these aircraft often have sufficient onboard stabilization that anyone can learn to pilot them without advanced training or skills. These aircraft are still new, and like in the early days of manned aviation, these aircraft are mostly used to gain an aerial perspective, with the most common use case being a "camera drone." There are also studies on the application of UAVs in the role of autonomous cargo carriers. The availability of these airframes has also benefited academia with many researchers diving into advanced control techniques for the automated processes, often searching for an optimal power solution to a maneuvering problem or studying autonomous decision making and path-finding [10–13].

Additionally, as the demand for these aircraft increases, the diversity of the market has also increased. Where there used to be a large distinction between fixed-wing UAVs, which were used for entertainment, and multi-rotor UAVs, which were used as camera drones or cargo carriers, vertical takeoff and landing (VTOL) UAVs are also starting to enter the market. These airframes take off vertically like a multi-rotor, but then as they accelerate forward they transition to more efficient wing-born flight [14–17].

With the diverse application of aerial vehicles in mind, it is easy to appreciate the complexity in the discipline of aircraft design. When a new aircraft is being created, the process of determining the optimal configuration to accomplish the design mission is non-trivial; it is even more complicated to determine the optimal placement of individual components onboard the airframe for each configuration. A team designing an aircraft typically has a set of requirements to optimize for, and no clear way to decide on the optimal configuration before running computations.

For a conceptual aircraft's performance to be compared with alternatives a design mission is derived from the set of requirements and each configuration's performance is evaluated over the entire mission. The design is then refined or iterated upon using a variety of methods, eventually converging to an optimized solution. This process requires accurate models for the aircraft systems, weight estimations of individual components, and an accurate model of its flight dynamics [18–23]. At this stage in the design process when evaluating the aircraft's

flight characteristics, it is advantageous to be able to make speedy comparisons between design iterations, therefore lower fidelity models of the lifting surfaces can be used. The fine aerodynamic details can be evaluated further along in the design process. For decades, Potential Flow solutions have been used to make fast, accurate approximations of the pressure field generated by a flow. In the field of computational fluid dynamics (CFD), panel methods use Potential Flow solutions to approximate the flow around arbitrary bodies.

This paper focuses on the integration of the Vortex Lattice Method for finding Potential Flow solutions and permitting aerodynamic evaluation of lifting surfaces in the context of aircraft design.

1.2 Previous Contributions and Objectives

Potential flow refers to a simplified form of the Navier-Stokes (NS) equations under the assumption that the flow is inviscid and irrotational, which reduces the governing equations to Laplace's equation [24]. The governing equations of Potential Flow are given in equation 1.1. Panel methods construct solutions by superimposing elementary solutions to Laplace's equation such as sources, doublets, and vortices distributed over the surface of a body [25]. Despite the limitations of being inviscid and irrotational, panel based solvers are commonly used since they have an inherent advantage over full three-dimensional NS solvers as fundamentally, they require less computational resources to run. A mesh for a NS solver encompasses the volume surrounding an object, but a panel based solver only requires a mesh covering the surface of the object being analyzed [26–28].

$$\frac{\partial V_x}{\partial x} + \frac{\partial V_y}{\partial y} + \frac{\partial V_z}{\partial z} = 0 \tag{1.1}$$

The Vortex Lattice Method (VLM) is a well known method for the determination of the characteristics of lifting surfaces, within the restrictions of Potential Flow. The method itself is described in detail in Chapter 2, but briefly it consists of overlaying the mean camber-surface of

a thin object with a series of horseshoe vortex segments, with the trailing edges extended downstream. In comparison to its three-dimensional siblings, source and doublet solvers, VLM simplifies the geometry by representing lifting surfaces as an infinitely thin mesh, typically across the mean camber line, and therefore neglects thickness effects. Because of this simplification, the method cannot capture the effect of thickness and therefore will only compute the induced component of drag, excluding the profile drag of the body since the surface is taken to have zero thickness. In addition to easier geometry processing with VLM, each individual computation when finding the solution to a VLM model is less computationally expensive than a source and doublet panel method since the velocity induction equations for those elements utilize trigonometric and logarithmic calculations in comparison to the vector operations necessary for a vortex segment [25].

The name VLM was first used in a 1948 paper by Hasselman and Riegels [29]. NASA then developed and released the source code for a VLM solver in 1971 to expedite its technical development [30]. The fundamental process underlying VLM has been used to model the performance of lifting surfaces since Prandtl's Lifting Line theory was introduced in 1918 [31], but as computational power has progressed, the advantages provided by VLM have become less valuable. With increased computational power, many research codes have either moved to directly solving flow-fields iteratively [32] or to evaluating three dimensional geometry using panel methods which can model thickness. Modern applications of VLM can be found in softwares such as Athena Vortex Lattice (AVL), OpenVSP VSPAERO's VLM solver, and Tornado VLM. AVL is a free software that was developed around 1989 for the analysis of simple configurations using a pure VLM solver [33]. OpenVSP is an aircraft design utility developed by NASA in 2012 and as of July 3, 2025 it is still receiving updates [34]. OpenVSP has methods for evaluating mass properties, performing structural analysis, and determining the aerodynamic performance of a configuration. The aerodynamic analysis package used in OpenVSP provides users with the option to find a solution using linear strength source and doublet panels or to apply a VLM solver to the lifting surfaces. OpenVSP VSPAERO includes an iterative wake relaxation procedure to align the trailing wake with local flow, improving predictions at moderate to high angles of attack. Tornado VLM was developed by Tomas Melin in 2000 as a

Matlab based research code for the analysis of aircraft flight dynamics, and it was later moved to Python [35–37].

In modern work, the most common use cases for VLM are extensions to unsteady flow [38–42]. Unsteady conditions typically arise from sudden gusts during flight, or due to alterations in the geometry itself, such as a flapping wing. VLM's simple geometry representation greatly expedites the modeling process when the geometry is being altered at each timestep. For lifting surfaces with sharp leading edges at high angles of attack, the formation of leading edge vortices greatly supplement the lift generated [43]. To model this in Potential Flow solvers such as unsteady VLM, one common practice is to apply a wake to the leading edge in addition to the trailing edge [44]. Alternatively, analytic corrections for the leading edge suction can be applied to more closely match experimental results [45]. The combination of unsteady VLM models and corrections for sharp leading edges have been used to perform analysis on rapidly pitching aircraft and flapping insect wings [46].

Aircraft design is an inherently iterative process. An initial geometry is proposed, analyzed for performance, and then refined based on the results [18]. Due to these frequent geometry changes, VLM is an excellent choice for evaluating an aircraft's aerodynamic performance during the sizing process. The goal of this work is to incorporate a VLM aerodynamic solver into an aircraft sizing framework for rapid and accurate evaluation of a configuration's performance during sizing iterations.

Chapter 2

Vortex Lattice Method Formulation

2.1 Vortex Lattice Method

The Vortex Lattice Method places horseshoe vortex filaments with different strengths across the wing to allow for the determination of the induced velocities necessary to enforce the no-penetration boundary condition. These induced velocities can then be used to calculate the differential pressure on a thin lifting surface and therefore the aerodynamic forces and moments. The velocity induced by a vortex segment is given by the Biot-Savart law:

$$V = \frac{\Gamma}{4\pi} \frac{dl \times r}{|r|^3} \tag{2.1}$$

In equation 2.1, V is the velocity induced by the vortex segment, Γ is the circulation strength of the vortex segment, dl is the length of the vortex segment, and r is the distance from the vortex segment to the location at which the induced velocity acts. Since the velocity induced by a vortex can be specified at a point using one vortex by solving for the required circulation, it follows that for a system of vortices, the velocity at a number of points equal to the number of vortex segments can have their velocities determined. The essence of the vortex lattice method is arranging a series of vortex segments over a lifting surface and then solving for the circulation required to force the flow around the lifting surface.

Solving for the circulation strengths is done by enforcing the no-penetration boundary condition, meaning that the flow is not permitted to have velocity normal to the lifting surface. A description of the geometry utilized for these computations can be found in section 2.2. The linear algebra formulation of the system of equations procured from applying this process is:

$$A\Gamma - \hat{b} = 0 \tag{2.2}$$

$$\hat{b}_i = \hat{n}_i \cdot V_\infty \tag{2.3}$$

The vector $\hat{b}$ is the component of the free-stream velocity normal to the panel's surface, and A is the geometry influence matrix, which contains the influence of each panel on every control point. The entries in A are the normal component of the induced velocity divided by Γ. The influence matrix of an aircraft with multiple lifting surfaces takes the form shown in equation 2.4 where A_{wt} is the influence of the wing on the tail, A_{tt} is the influence of the tail on itself, A_{tw} is the influence of the tail on the wing, and A_{ww} is the influence of the wing on itself.

$$A = \begin{bmatrix} A_{wt} & A_{tt} \\ A_{ww} & A_{tw} \end{bmatrix} \tag{2.4}$$

To solve for the circulation strength required to enforce the no-penetration boundary condition, equation 2.2 is rearranged:

$$A^{-1}\hat{b} = \Gamma \tag{2.5}$$

Equation 2.5 requires the inversion of the geometry influence matrix. The computation of this matrix inversion, while not the limiting factor for the speed of the solver, can be memory intensive. To ensure that a solution can be obtained without excessive memory requirements, an iterative solver is called if the total vehicle's panel count exceeds 2500. As is common with vortex lattice solvers, the generalized minimal residual (GMRES) algorithm [47] was selected for these high-memory cases.

An additional boundary condition is applied in the form of wake attachment. The wake represents the flow leaving the lifting surface and traveling downstream. Despite the seemingly simple goal, placing the wake in a way that follows closely to experimental results requires

iteratively solving for location of points between the trailing edge and the distant wake until there is zero pressure jump across the wake.

Alternatively, the wake can be defined as a flat line extending from the trailing edge of the lifting surface to the distant point. This method requires an additional step in geometry processing as the flow direction must be included in the computation of the distant wake points, but it is still much less computationally expensive than the iterative solution.

A third method for attaching the wake is to model it as completely flat, and invariant to flow conditions. This method is by far the simplest, but it is also the least accurate. For the vortex lattice geometry solver developed in this work, the wake is taken as the second option: a flat line oriented with the free-stream extending to a distant point.

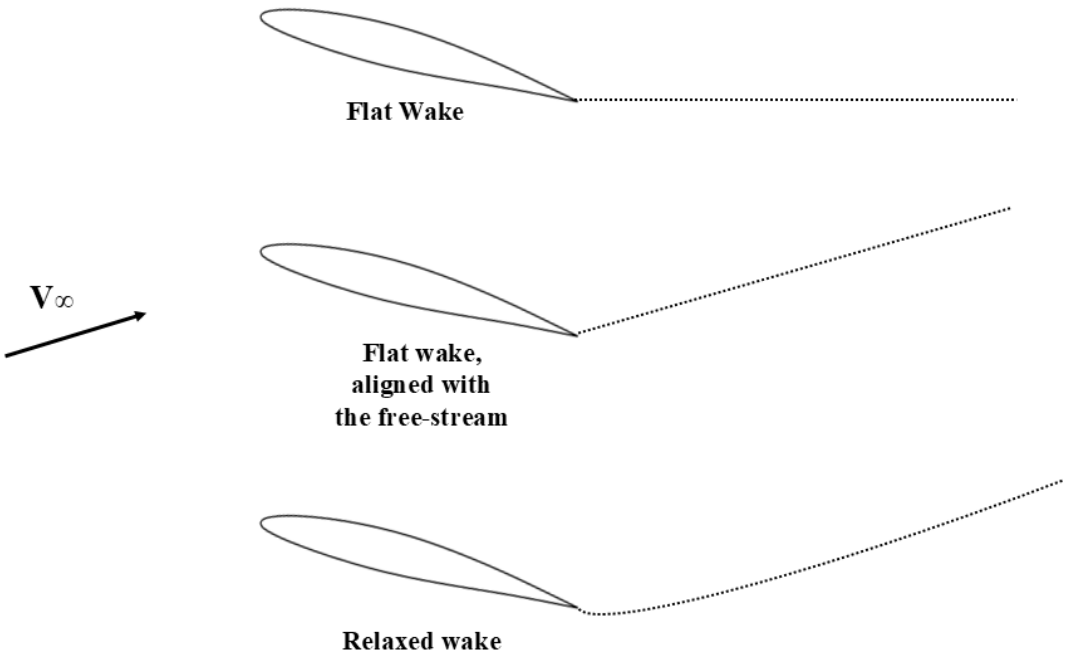

Figure 2.1: Methods for wake attachment.

2.2 Geometry processing

To construct the arrangement of horseshoe vortices and control points required for computations, a mesh of quadrilaterals is overlaid on the lifting surfaces. The geometry input can be

either the individual strips used by the Parametric Energy-based Aircraft Configuration Evaluator (PEACE) as part of the geometry model, or it can be the general geometry definition of the wing section consisting of taper, sweep, dihedral, and the wing's airfoils at the beginning and end of the lifting surface. Either method can be used for computation, and the results will be identical. Any advantage for one model or the other is dependent upon the total panel number and therefore runtime. The method utilizing individual wing sections will be advantageous for wings with several well-defined trapezoidal wing areas, whereas if the geometry has a large number of constantly varying sections, the mesh resulting from the pre-computed PEACE strip definition may be essential for efficient computations. If the wing is chosen to have different airfoils along the span, the airfoil coordinates are either computed by PEACE before the VLM solver is run, or a constant linear transition between the airfoil cross-sections is assumed and all intermediate camber values are written as a linear combination of the two airfoils.

Whichever method is chosen for the wing definition, the remaining steps in the mesh creation process are identical. A series of strips are defined along the wing. Each strip is oriented using the wing's twist, taper, dihedral, and camber, then chordwise panels are defined on each strip with the coordinates of the points used for computations stored in the panel's object.

Each chordwise panel is a quadrilateral, and each panel has a bound vortex, two trailing wake vortices, a normal vector, and a control point. A panel has been defined in terms of its four edges. Since the panel is flat, the normal vector is defined as the cross product of two adjacent edge vectors. The panel center is the average of the four corners, and the control point is calculated using linear combinations of the four edge points, placing it at centerline of the panel along the 3/4 chordline. The control point is placed at the 3/4 chordline based on the combination of thin airfoil theory with the normal free-stream velocity. By joining these expressions, it is determined that there is zero net velocity at a distance c/2 from the bound vortex where c is the panel's chord [48].

The bound vortex's coordinates are calculated by writing a point along the left and right sides at the quarter-chord using a linear combination of the front and back corners. Then the beginning and end of the vortex are positioned at these points along the panel's quarter-chord

line. The trailing vortices are defined as vectors formed between the left and right bound vortex points and a point twenty times the local chord downstream of the trailing edge of the lifting surface. If P_{FL}, P_{FR}, P_{BL}, P_{BR} are taken to be the front left, front right, back left, and back right points of the quadrilateral, the following expressions can be used to determine the location of the required points.

$$P_{CP} = \frac{1}{4}(P_{FL} + P_{FR} + 3P_{BL} + 3P_{BR}) \tag{2.6}$$

$$P_{VL} = \frac{1}{4}(3P_{FL} + P_{BL}) \tag{2.7}$$

$$P_{VR} = \frac{1}{4}(3P_{FR} + P_{BR}) \tag{2.8}$$

$$P_c = \frac{1}{4}(P_{FL} + P_{FR} + P_{BL} + P_{BR}) \tag{2.9}$$

$$\hat{n} = |(P_{FR} - P_{FL}) \times (P_{FL} - P_{BL})| \tag{2.10}$$

$$P_{WL} = P_{BL} + 20 \begin{bmatrix} -\cos\alpha\cos\beta \\ \sin\beta \\ -\sin\alpha \end{bmatrix}^T c \tag{2.11}$$

$$P_{WR} = P_{BR} + 20 \begin{bmatrix} -\cos\alpha\cos\beta \\ \sin\beta \\ -\sin\alpha \end{bmatrix}^T c \tag{2.12}$$

In the above expressions, P_{CP} is the control point, P_{VL} and P_{VR} are the left and right endpoints of the bound vortex, P_{WL} and P_{WR} are the ends of the wake, c is the local chord of the lifting surface. P_c is the center of the panel and $\hat{n}$ is the normal vector of the panel, α is the geometric angle of attack of the lifting surface and β is the geometric side slip angle of

the lifting surface. The factor of 20 places the ends of the wake sufficiently far from the wing for the flow to become realigned with the free-stream. Adjusting this value has little impact permitting that the wake distance does not become small when compared with the size of the lifting surface.

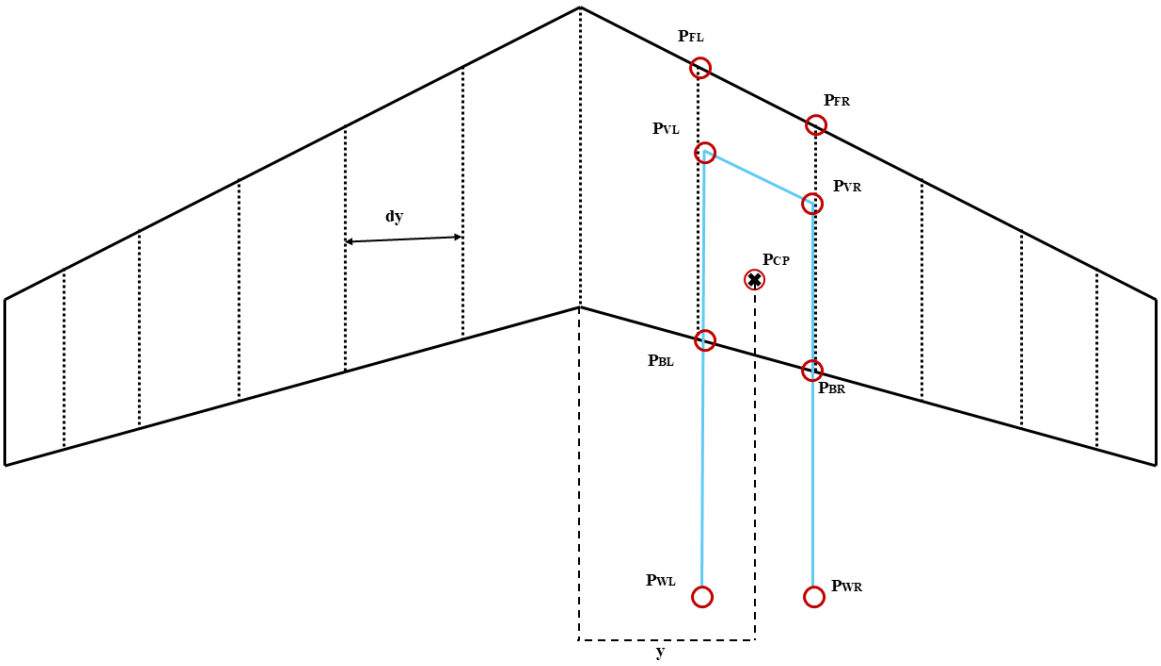

Figure 2.2: Typical wing geometry with one chordwise panel.

In cases where the geometry or load changes more rapidly across some areas of the lifting surface, it is advantageous to have a higher density of panels in those locations for accurate modeling. Along the chord of a wing, the most important locations to capture are the leading edges and the trailing edges as those locations are where the flow first encounters and leaves the wing. The leading edge is also the location where the pressure of the flow changes the fastest. Because of these considerations, it can be advantageous to apply a clustered panel distribution with higher concentrations at the leading and trailing edges. The mesh generation implemented in the current model allows for both constant panel spacing and clustered panel spacing.

2.3 Vortex Lattice Solution

Once all the requisite geometry computations have been completed the full mesh can be passed to the VLM solver. The first and most computationally expensive step in the process is the formation of the geometry influence matrix A. The geometry influence matrix is a O(n^2) operation where n is the number of control points. Each individual computation of the Biot-Savart equation is not expensive since it is composed of vector operations, however when the total number of panels is considered, this step is the most expensive of the process.

The assembly of the geometry influence matrix requires finding the velocity induced by every vortex segment on every control point using the Biot-Savart relations discussed in Section 2.1. Completing the computation for a single vortex segment on a single control point is not particularly taxing, the high cost arises when the total number of panels is considered.

While the geometry influence matrix is being computed, the three components of the local induced velocities returned from the Biot-Savart relation are stored to aide in the computation of the local x, y, and z component velocities during the evaluation of the forces across the aircraft. As discussed in Section 2.1, the system of linear equations is then solved by matrix inversion to determine the circulation strengths of each vortex segment, the lift for each panel and the drag for each strip. The cross product of the lift per panel can then be taken about a point, either the aircraft's reference frame origin or the local quarter-chord of the lifting surface, to determine the moments resulting from the lift distribution. The expressions for the vertical force (lift) and lateral force (side-force) per panel are given in equations 2.13 and 2.14 where dy is the length of the panel's bound vortex, ρ is the density of the free-stream, $\hat{k}$ vertical unit vector of the aircraft's reference frame and $\hat{j}$ is the lateral unit vector. V_{local} is determined by summing the three components of the induced velocity at that control point with the free stream velocity.

$$F_z = (\rho\Gamma(V_{local} \times dy)) \cdot (\hat{k}) \tag{2.13}$$

$$F_y = (\rho\Gamma(V_{local} \times dy)) \cdot (\hat{j}) \tag{2.14}$$

2.4 Compressibility Corrections

As the properties of the flow are not actually computed for the air surrounding the lifting surface, the classical vortex lattice solution is only valid for incompressible flow. Below mach 0.3 density changes over the body can be considered to be small; while in contrast, above 0.3 it is necessary to account for the changes in the flow's density. The first process to correct the vortex lattice solution for compressibility is known as the similarity laws. The similarity laws consist of scaling the aircraft's geometry by the Prandtl-Glauert correction factor β_{PG} in order to get a new geometry which can be evaluated to derive the performance of the original wing when in compressible flow conditions.

$$\beta_{PG} = \sqrt{1 - M_{\infty}^2} \tag{2.15}$$

Following this methodology, any point in the geometry can be related to its new location in the stretched geometry by the expression:

$$\hat{P_C} = [\frac{P_{IC_x}}{\beta_{PG}}; P_{IC_y}; P_{IC_z}] \tag{2.16}$$

Where $\hat{P_C}$ is the stretched geometry and $P_{IC_{xyz}}$ are the coordinates of the initial geometry. In addition to scaling the geometry, the angles of the oncoming flow must be adjusted.

$$\alpha' = \alpha\beta_{PG} \tag{2.17}$$

$$\beta' = \beta\beta_{PG} \tag{2.18}$$

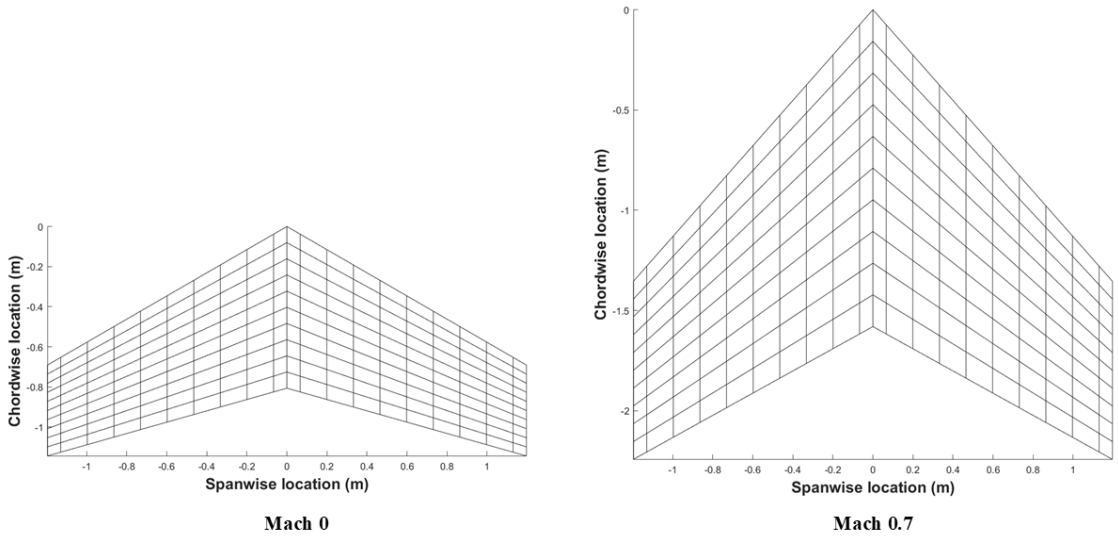

Figure 2.3: A lifting surface before and after geometry scaling.

For comparison, the Prandtl-Glauert compressibility correction was also implemented as an alternate method for the correction to compressible flow. To utilize this method, the solution is determined for the original, unmodified, geometry at an incompressible mach number, typically mach 0, then the following correction is applied:

$$C_p = \frac{C_p}{\beta_{PG}} \tag{2.19}$$

Since the lift coefficient and drag coefficient are known to be directly proportional to the pressure coefficient, the circulation Γ itself is scaled by the correction factor. The alternative to this method would be to apply the β_{PG} factor at each station's C_L, $C_{m_{c/4}}$ and C_{di} independently. By applying the Prandtl-Glauert correction directly to the circulation, the pressure distribution across the lifting surface is scaled before any forces or moments are computed; therefore, no additional adjustments are required for each independent coefficient.

2.5 Drag Calculation

Aircraft drag is most often divided into profile drag C_{dP}, induced drag C_{di}, and wave drag C_{dw}. Profile drag consists of the drag from skin friction C_k and pressure drag C_{d_p}. Pressure drag is the force produced by an object that obstructs a flow and causes a change in pressure that

is unfavorable to the direction of travel. The drag caused by moving a body through a flow is captured in 2D airfoil data and can be combined with induced drag calculations to determine the total pressure drag contribution.

$$C_D = C_{d_p} + C_{di} + C_{dw} \tag{2.20}$$

After the vortex lattice solution is found, a lookup table for C_{d_n} = F(C_{L_n}) is utilized where n is the chordwise row of panels along a lifting surface. This, of course, does require the user to have precomputed airfoil data. Most often for PEACE, XFOIL is utilized, and for the transition airfoils, the profile drag is taken to be a linear combination of the profile drag solution of the airfoils at the beginning and end of the wing section. Wave drag is a phenomenon originating from the formation of shock waves during transonic and supersonic flow and is currently not captured by the present model.

2.6 Induced Drag Calculation

Since the Vortex Lattice Method assumes that the lifting surface has zero thickness, it is not capable of directly determining the total pressure drag of a lifting surface; however, it is capable of directly computing the induced drag. For the present model, the induced drag is found using the Treftz-Plane method.

$$\alpha_i(y_n) = \frac{1}{4\pi V_\infty} \int_{-b/2}^{b/2} \frac{\frac{d\Gamma}{dy}}{y_n - y} dy \tag{2.21}$$

$$C_{di}(y) = \frac{2}{V_\infty S} \int_{-b/2}^{b/2} \Gamma(y)\alpha_i(y) dy \tag{2.22}$$

To apply this equation, the circulation per unit span is first computed, then passed to a function which computes the spanwise derivative. For the computation of the derivative, a fourth order central difference scheme is applied for interior points.

$$\frac{du}{dx}\Big|_i = \frac{-u_{i+2} + 8u_{i+1} - 8u_{i-1} + u_{i-2}}{12\Delta x} \tag{2.23}$$

For the initial two points and the final two points, second-order single-sided difference schemes are applied. For the ends of the wing where sufficient terms on either side of the station are unavailable.

$$\frac{du}{dx}|_i = \frac{-3u_i + 4u_{i+1} - u_{i+2}}{2\Delta x} \tag{2.24}$$

$$\frac{du}{dx}|_i = \frac{3u_i - 4u_{i+1} + u_{i+2}}{2\Delta x} \tag{2.25}$$

When combined into the derivative stencil matrix, the form is:

$$\frac{d\Gamma}{dy} = D_1\Gamma \tag{2.26}$$

$$D_1 = \frac{1}{2\Delta x}\begin{bmatrix} -3 & 4 & -1 & 0 & 0 & 0 & \cdots & \\ 0 & -3 & 4 & -1 & 0 & 0 & \cdots & \\ \frac{1}{6} & \frac{-8}{6} & 0 & \frac{8}{6} & \frac{-1}{6} & 0 & \cdots & \\ & \ddots & \ddots & \ddots & \ddots & \ddots & & \\ & & \ddots & \ddots & \ddots & \ddots & \ddots & \\ & \cdots & 0 & \frac{1}{6} & \frac{-8}{6} & 0 & \frac{8}{6} & \frac{-1}{6} \\ & \cdots & 0 & 0 & 3 & -4 & 1 & 0 \\ & \cdots & 0 & 0 & 0 & 3 & -4 & 1 \end{bmatrix} \tag{2.27}$$

To ensure that this expression always provides an accurate output, it is necessary that the minimum number of span-wise panel strips for any lifting surface should be ten, and the solver will display warnings if a fewer number of panels is utilized. This is considered to be an adequate restriction because a solution with fewer than ten spanwise strips will likely result in low-resolution data.

2.7 Fuselage forces and moments

Because the fundamental process of the Vortex Lattice Method assumes a thin lifting surface, it is not suited to the modeling of blunt, nonlifting bodies such as fuselages. Therefore, there must be a separate process for the characterization of the aerodynamics of any non-lifting bodies. For the incorporation of fuselages in the present model, the user is required to enter a reference curve for the fuselage forces and moments as a function of the angle of attack, side slip angle, and mach number; then the effects of the fuselage are added to the total forces and moments acting on the aircraft. This means that the computational results found by the vortex lattice solver will not include the effect of the fuselage on the wings and that the fuselage model will not include the effects of the wings on the fuselage. While this may be considered adequate for aircraft sizing, it may be desirable to integrate a source and doublet solver for fuselage forces and moments, as well as to capture the wing-body interaction.

Chapter 3

Aerodynamic Solver Incorporation into Aircraft Sizing Framework

3.1 PEACE Aircraft Sizing Framework

The Parametric Energy-based Aircraft Configuration Evaluator (PEACE) is a MATLAB-based framework developed at Vehicle Systems, Dynamics and Design Laboratory (VSDDL) to facilitate the design, sizing, and optimization of novel aircraft configurations. It uses a generalized energy-based approach to the modeling of propulsion systems which enables the modeling of diverse propulsion concepts and extends its applicability to wing-born aircraft, rotary wing aircraft, buoyant lift aircraft, or any combination [49]. The PEACE sizing process has been demonstrated for numerous propulsion architectures including all-electric, hydrogen proton exchange membrane fuel cell (PEMFC), hybrid electric, and pure gas-burning engines. [50–52].

The eXtended Design Structure Matrix (XDSM) [53] workflow in PEACE, illustrated in Fig. 3.1, uses nested loops to first converge the operating energy mass (OEM) then iterate on the aircraft maximum takeoff mass (MTOM) in the outer loop.

- **Geometry Updater**: At each iteration of the *OEM converger* this module arranges the configuration's geometry based on high-level aircraft design variables and propagates changes to the downstream modules.
- **Aero-Propulsive Performance Model (APPM) Updater**: Calculates the propulsion and aerodynamic parameters so that they can be assessed by downstream modules. This module contains the VLM solver for computing the forces and moments produced by lifting surfaces.

- **Stability and Control (S&C)**: Assesses the stability of the configuration. This module evaluates aircraft controls such as thrust vectoring, blade pitch, and control surface deflections.

- **Power Sizer**: Evaluates the configuration's performance during nominal and off-nominal flight conditions. Configuration specific relations between the propulsion system and energy storage mechanisms are evaluated at the most constraining design conditions to determine the energy requirements.

- **OEM and Mass Properties Calculator**: Uses configuration specific relations to determine individual component's mass properties, then determines the OEM of the vehicle by summing the masses of all the vehicle's components. The vehicle's center of gravity location and inertia tensor are computed by taking weighted averages and by applying the parallel axis theorem respectively.

- **Net Available Energy Mass (NAEM)**: NAEM is defined as the difference between MTOM and the sum of OEM and the payload mass. NAEM is equal to the sum of all the energy sources onboard the configuration.

To determine the performance of the configuration, the **Mission Analyzer** is used. The vehicle is trimmed at a series of points for each mission segment. This process computes the rate of energy consumption for every flight condition using the propulsive power requirement. The Mission Analyzer also computes the required and excess energy masses based on the rate of energy consumption. [54]

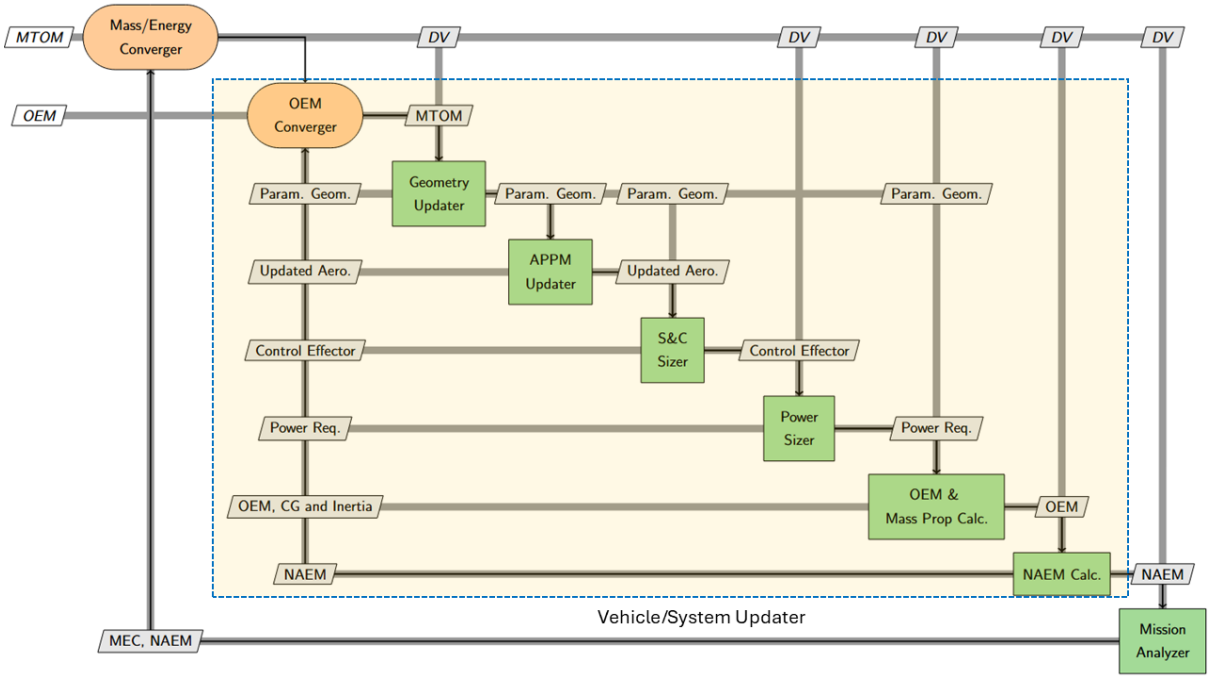

Figure 3.1: XDSM representation of the PEACE aircraft sizing and mission analysis framework [52].

3.2 Aerodynamic Model Integration

When the aerodynamic geometry changes during a sizing iteration, the APPM Updater module is run, and a sweep is conducted for a range of angles of attack, sideslip angles, and mach numbers using the VLM solver for lifting surfaces and lookup tables for non-lifting bodies. Afterwards, the data for the lift coefficient, induced drag coefficient, and the moment about the local quarter-chord are stored in lookup tables. During the mission segments, these lookup tables are queried for different flight conditions, and combined with the fuselage data and two-dimensional airfoil data to compute the aerodynamic forces and moments for the configurations using the methods described in Chapter 2.

3.3 Control Surface Deflections for Determining the Trim Solution

Unlike aerodynamic solvers that utilize full thickness bodies, the 2.5D/mean camber surface of the VLM can represent the deflection of control surfaces with ease. Since the method is fundamentally based on enforcing the no-penetration and Kutta boundary conditions, to model

the deflection of a control surface, the only requirement is that the mesh be modified to follow the mean camber surface of the new airfoil. It is worth noting that since the VLM does not capture flow separation at high angles of attack due to the absence of viscosity terms in the governing equations, it is also not able to capture the decreased effectiveness of control surfaces with high deflection angles. If this method is utilized, empirical corrections for the reduction of control surface effectiveness at high degrees of deflection are applied.

Alternatively, for rapid iterations while trimming the aircraft at different flight conditions, it is advantageous to apply modifications to the wing section's force and moment coefficients using DATCOM's empirical approach. After the VLM solution is found for the spanwise lift, drag, and moment coefficients, a factor is applied based on the empirical results to the relevant spanwise strips [55–58].

Chapter 4

Results

To ensure the VLM solver framework is robust, several configurations were tested. The results of the VLM framework were compared to the solution from industry standard aerodynamic solvers and experimental data to verify that the correct solution was reached. For comparison, the configurations were evaluated using FlightStream and OpenVSP VSPAERO's VLM solver. These solvers were chosen as they are known to produce trustworthy results when operated by an informed user. Additionally the VLM solver used in OpenVSP can be directly compared to the method developed in this work. FlightStream is a surface vorticity solver that models the thickness of lifting surfaces and non-lfiting bodies. Where appropriate, FlightStream was used to generate results for the complete aircraft configuration for the comparison.

4.1 Single Wing

In order to first validate the VLM solver, it was directly compared to experimental results [59]. To emphasize the separation of this model from a standard lifting line or strip theory solution, a wing with a high sweep of 45° and an aspect ratio of 5 was chosen. Experimental results are found in Weber et al. where the wing was analyzed in the Royal Aircraft Establishment's wind tunnel facility as part of a study investigating the pressure distribution of swept wings. The airfoil used in the relevant test case was the RAE 101 with a thickness to chord ratio of 12% with the maximum thickness occurring at 31% of the chord.

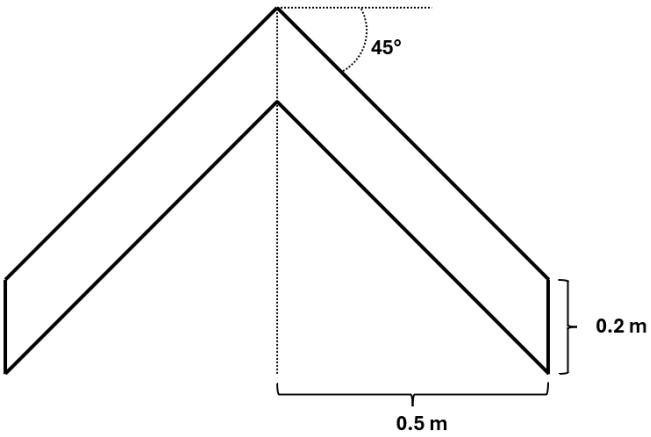

Table 4.1: Geometry properties.

Aspect ratio	5
Taper ratio	1
Wingspan	1 m
Root chord	0.2 m
Wing area	0.2 m^2

Figure 4.1: Geometry of the Swept wing.

For direct analysis of the spanwise distribution of forces, the local lift coefficients were compared. During the collection of experimental results, pressure at spanwise locations was computed from taps along the upper and lower surfaces of the airfoil. The integrated pressures were then used to compute the coefficient of lift at these stations. The spanwise lift distribution was computed using a vortex lattice solution of 20 spanwise panels and 10 chordwise panels for a total of 200 panels. The lift coefficient per unit span was determined by summing the chordwise circulations for each row of panels, then applying equation 4.1 to determine the local lift coefficient. The results for this analysis are presented in Section 4.2.

$$C_L(y) = \frac{2\Gamma}{qc_{local}} \tag{4.1}$$

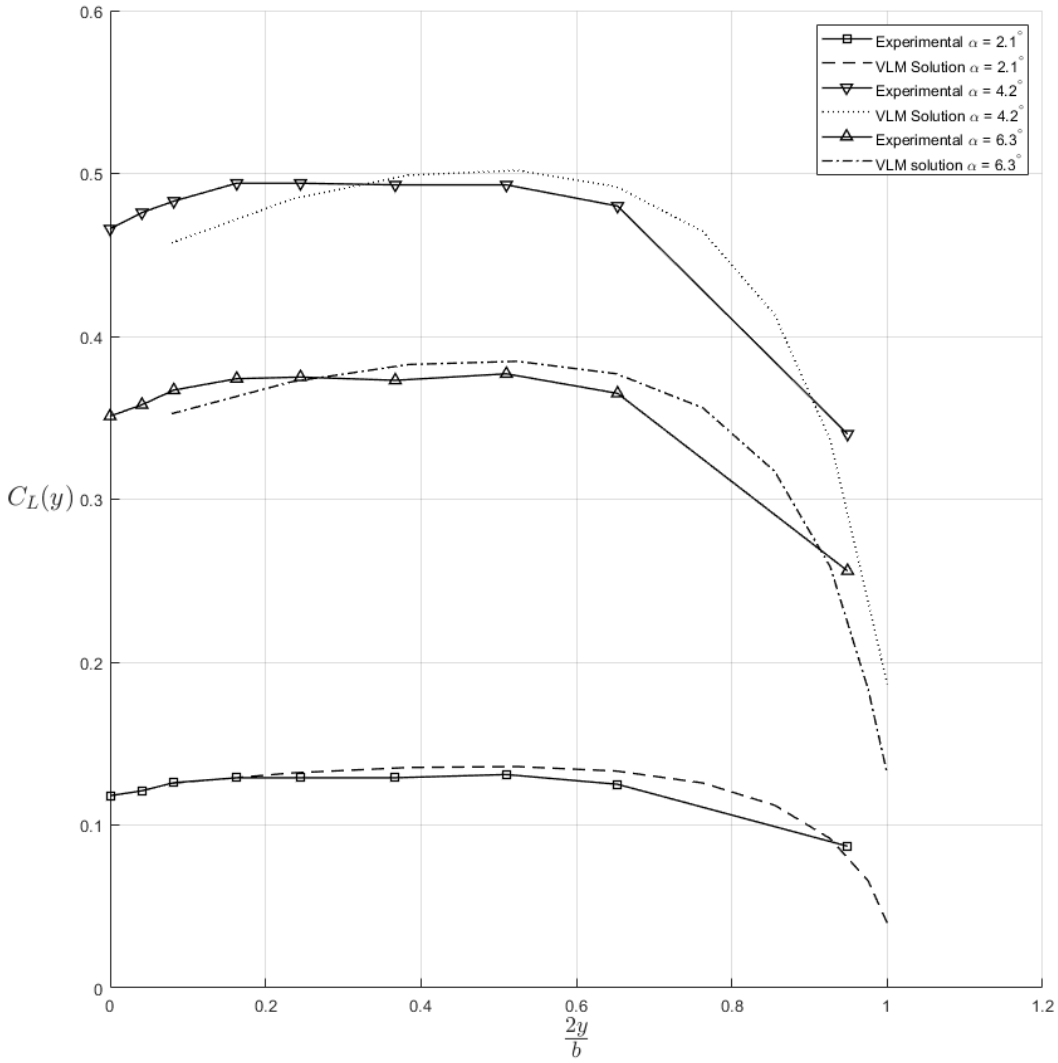

Figure 4.2: Coefficient of lift spanwise distribution.

As can be seen from the results in Fig. 4.2 and Fig. 4.3, the VLM solver developed for this project has a strong correlation with experimental results. It can also be concluded that as viscous corrections are not included in the pure VLM solution, as the angle of attack increases, the results begin to diverge from the experimental predictions. Despite this difference in physical modeling, the maximum error in the wing's C_L is 4.43%, and as is to be expected, this error occurs at the maximum tested angle of attack of $10.5°$.

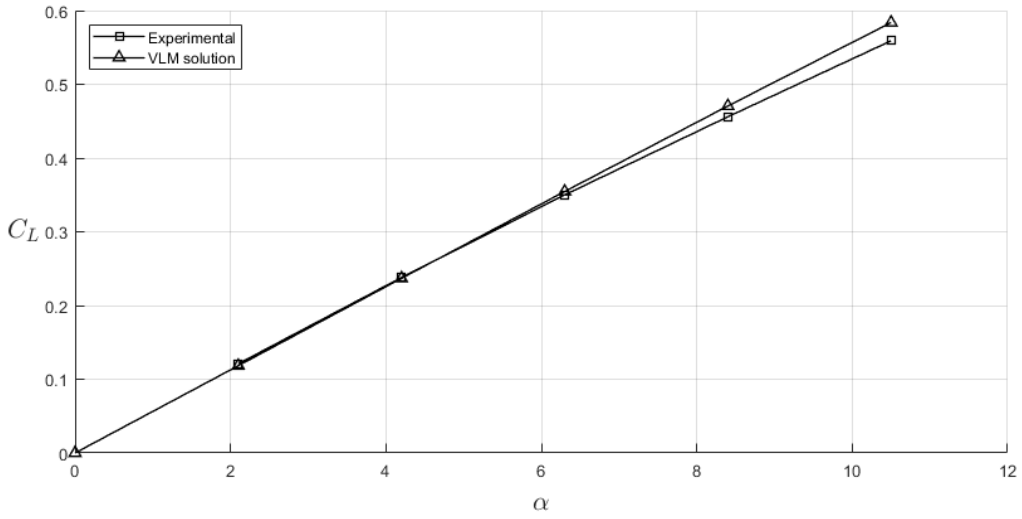

Figure 4.3: Coefficient of lift of the wing.

4.2 Tube-Wing Aircraft

To ensure the method would be expedient and numerically well behaved, a typical configuration which incorporates common design alterations was evaluated. The baseline for this configuration was the Boeing 737-800. It is referred to here as a ”Tube-Wing aircraft” because of its long cylindrical fuselage [60, 61]. This aircraft has a large, high aspect ratio wing with varied airfoils, taper ratios, and sweep angles. The wing and tail both have dihedral with the wing having several changes in the dihedral. By modeling these design features on a configuration with multiple lifting surfaces it is ensured that the model is able to evaluate the majority of configurations.

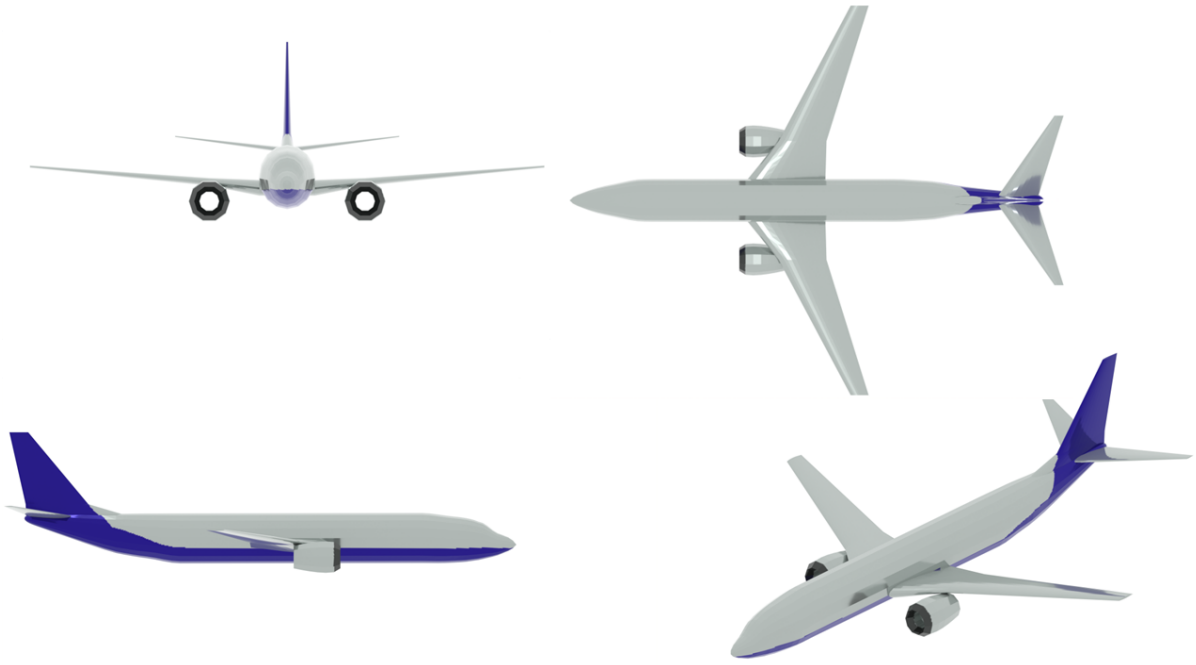

Figure 4.4: The Tube-Wing configuration [52].

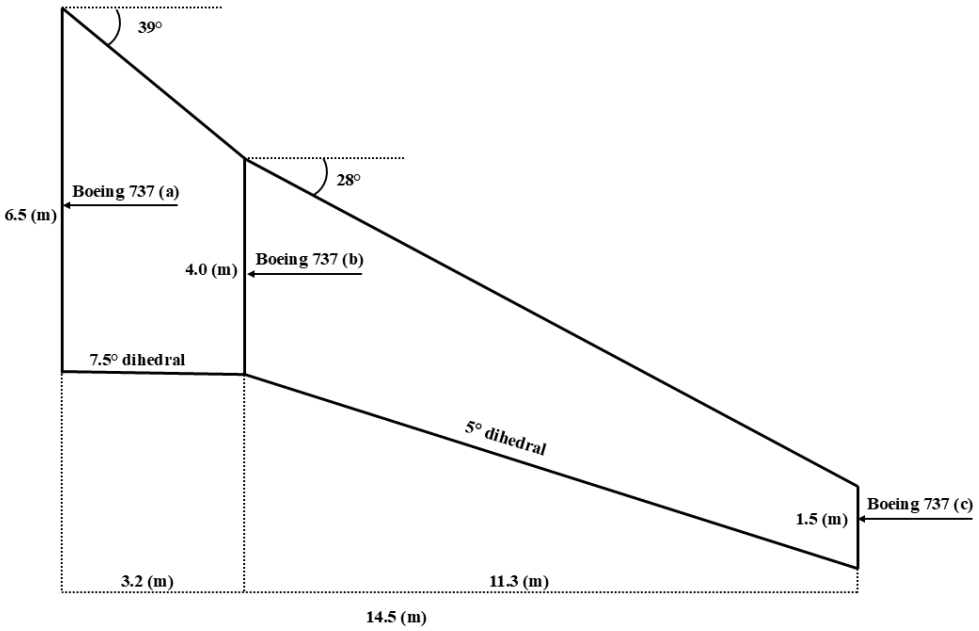

Figure 4.5: Wing of the Tube-Wing aircraft model.

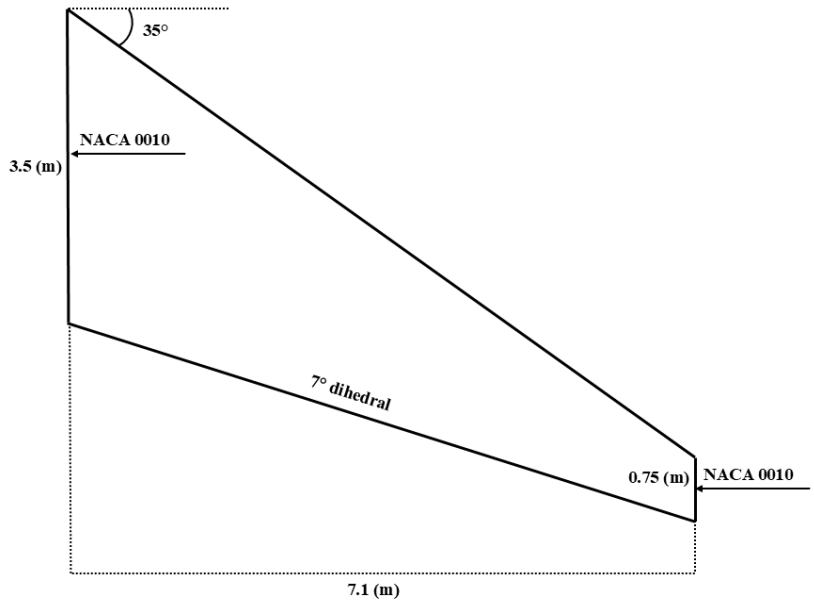

Figure 4.6: Horizontal stabilizer of the Tube-Wing aircraft model.

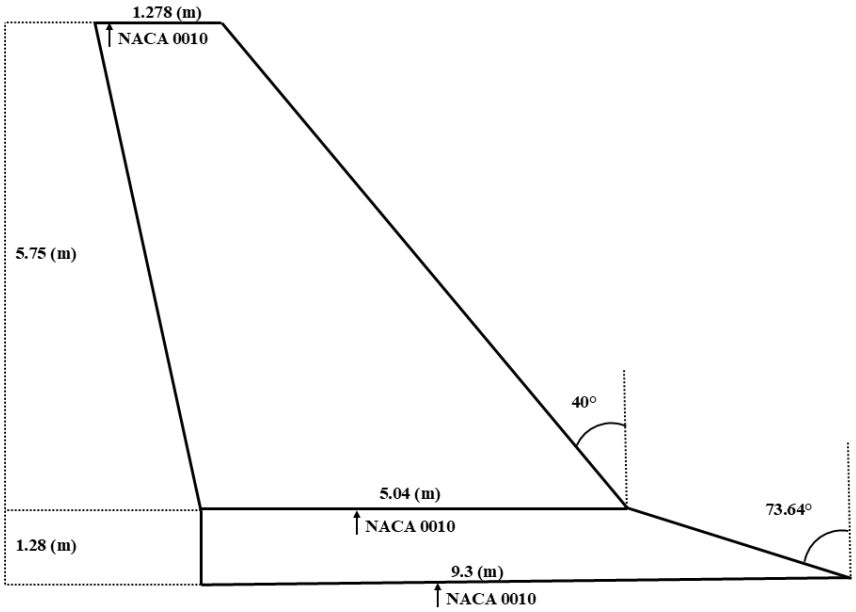

Figure 4.7: Vertical stabilizer of the Tube-Wing aircraft model.

The wing is defined in three sections, with the inner most section utilizing the (B737a) airfoil. The next section transitions from the (B737a) to the (B737b). Finally the outer most section transitions from the (B737b) to the (B737c). As is to be expected for VLM, the fuselage

and engine nacelles are not modeled in the solution. The mesh utilized also has a section connecting the two wings. By connecting the wings, the interaction between the lifting surfaces is more closely linked. There is much discussion in literature for the proper handling of this area, for this case the wings mesh will be evaluated as shown with no alterations made through post-processing [62, 63].

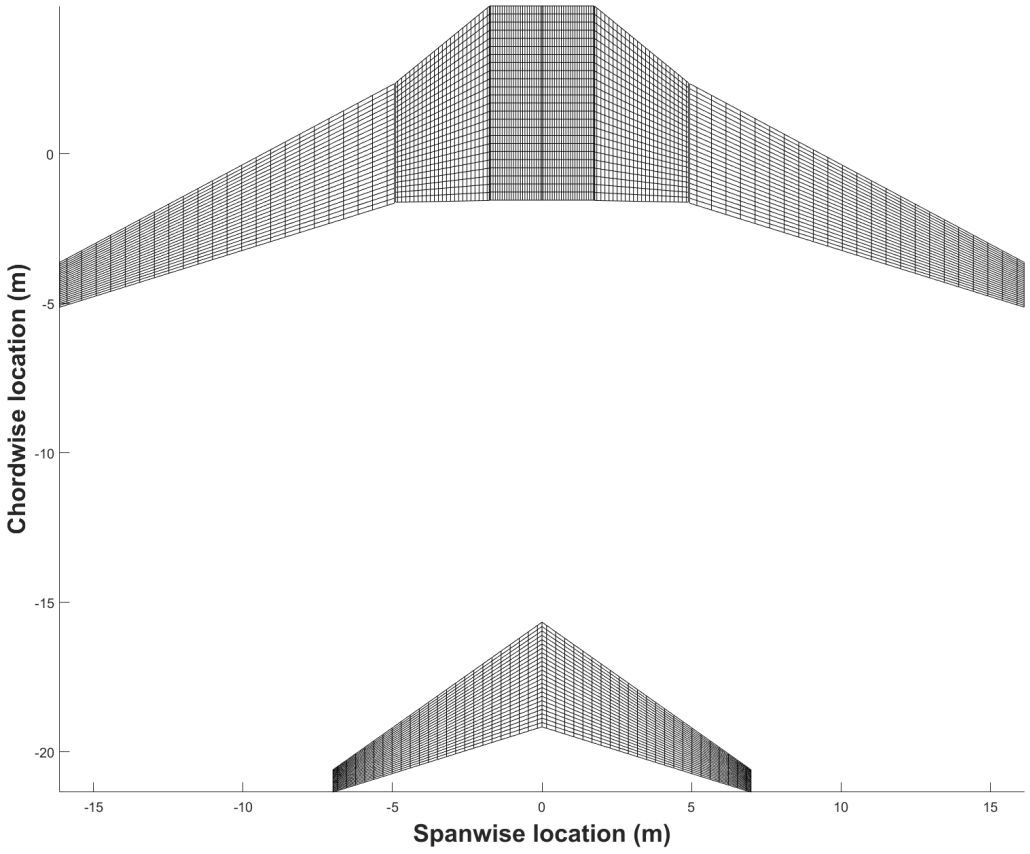

Figure 4.8: The VLM mesh for the tube wing aircraft.

First, a comparison was made between the performance of the present model and a OpenVSP VSPAERO solution found using the integrated VLM solver. By conducting this comparison, the performance of the present model can be benchmarked against a comparable solver, and differences in the underlying process can be explored. For this initial case the lifting surfaces of the tube wing configuration were analyzed.

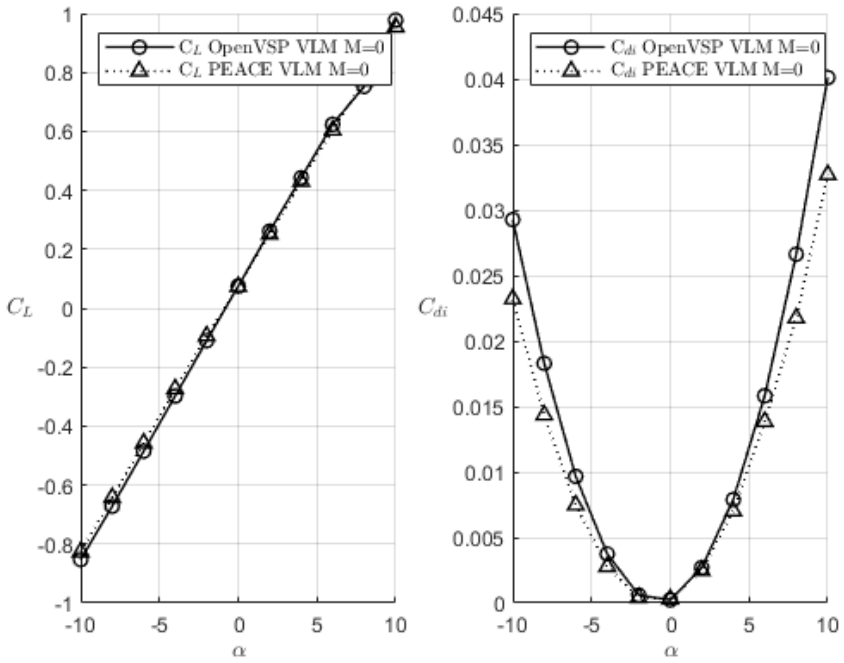

Figure 4.9: VLM results for a sweep of α and M = 0 on the tube wing aircraft's lifting surfaces.

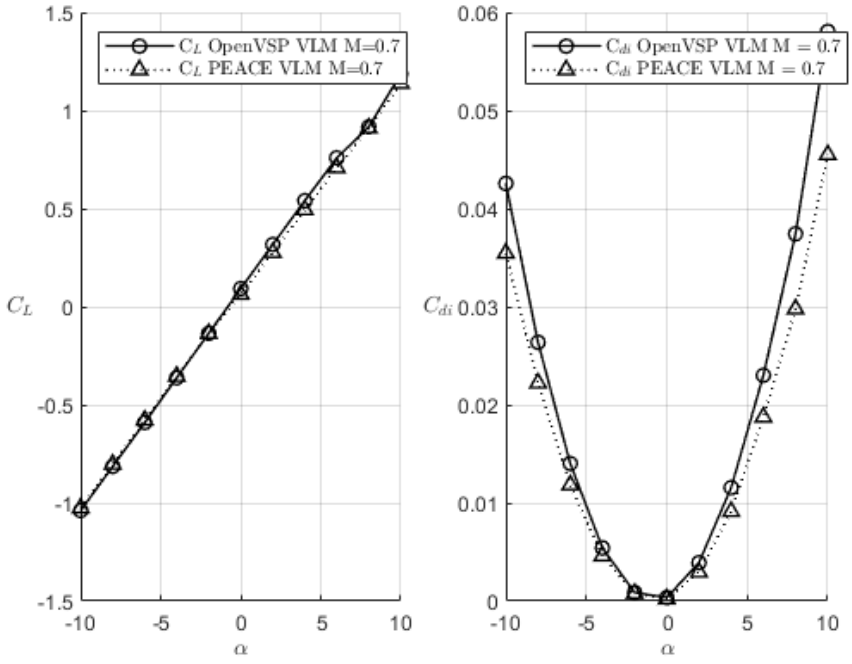

Figure 4.10: VLM results for a sweep of α and M = 0.7 on the tube wing aircraft's lifting surfaces.

Figure 4.9 and 4.10 provide the coefficient of lift and induced drag for the lifting surfaces of the tube wing configuration. These coefficients were chosen as they are the most direct output of a vortex lattice solution. The present model and OpenVSP VSPAERO's VLM solutions show good agreement in lift, the major discrepancies occur in drag computations. OpenVSP uses an iterative wake relaxation routine which is not applied in the present model. As the induced drag is computed using the Treftz-Plane method described in section 2.6 the results differ since the calculation is entirely dependent on the downwash of a given lifting surface. Since the iterative wake relaxation routine changes the downwash, it also causes a large difference in the final drag computations when compared to flat wake methods.

For the lift coefficient, the behavior is linear, as is expected for this system, but the OpenVSP solution has an anomaly at $\alpha = 8^{\circ}$. After an investigation into the cause, it was determined that this occurs when the wake from the wing makes contact with the horizontal stabilizer, passing near a control point. If an issue like this occurs, the user can alter the computational mesh to shift the location of the control points and trailing wakes, or discard the corrupted data points. Inconsistencies like this should alert the user to the possibility of wing-tail interference in the configuration.

Next, the method is compared to the results from FlightStream for the same vehicle. Two sets of data was generated from FlightStream, one set was for the entire configuration, the other was just for the fuselage in isolation. Inline with the procedure described in Chapter 2, the VLM solution was found, then the profile drag terms were added along with the effects of the fuselage to determine the vehicle's performance.

As can be seen by the curves shown in Fig. 4.11, the fuselage does not contribute significantly to the vehicle's lift and the pitching moment produced is small. This is expected for configurations where the fuselage is narrow in relation to the rest of the aircraft and is not shaped as a lifting body. Despite the lift and drag having small contributions, the drag coefficient of the fuselage is a significant fraction of the induced drag data presented in Fig. 4.9 and Fig. 4.10. It is also worth noting that the fuselage is producing a destabilizing pitching moment, which is to be expected for long cylindrical fuselages [18].

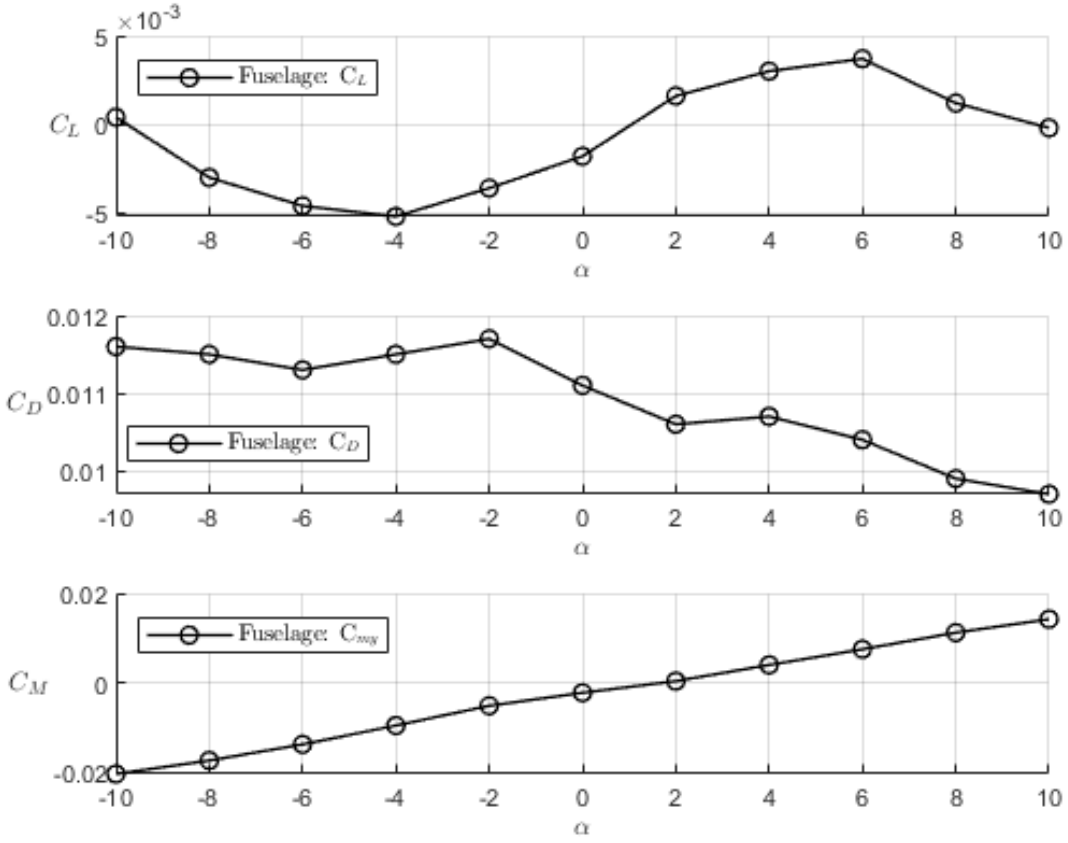

Figure 4.11: The tube-wing aircraft's fuselage force and moment curves.

Finally, all the data is assembled to provide the total forces and moments acting on the vehicle. The results for the full configuration at a compressible flow mach number can be found in Fig. 4.12. For the full configuration, the present model has a tendency to over-predict drag and under-predict the lift for most flight conditions. The non-linearity introduced into the lift coefficient curve originates from the fuselage aerodynamic curves, and as can be seen in Fig. 4.9 and Fig. 4.10. The pure VLM C_L output for the present model is linear. It can be observed that the pitching moment coefficient was well behaved, this can be explained by the fact that the presence or absence of the fuselage would have less impact on the chordwise pressure distribution that the spanwise pressure distribution of the aircraft.

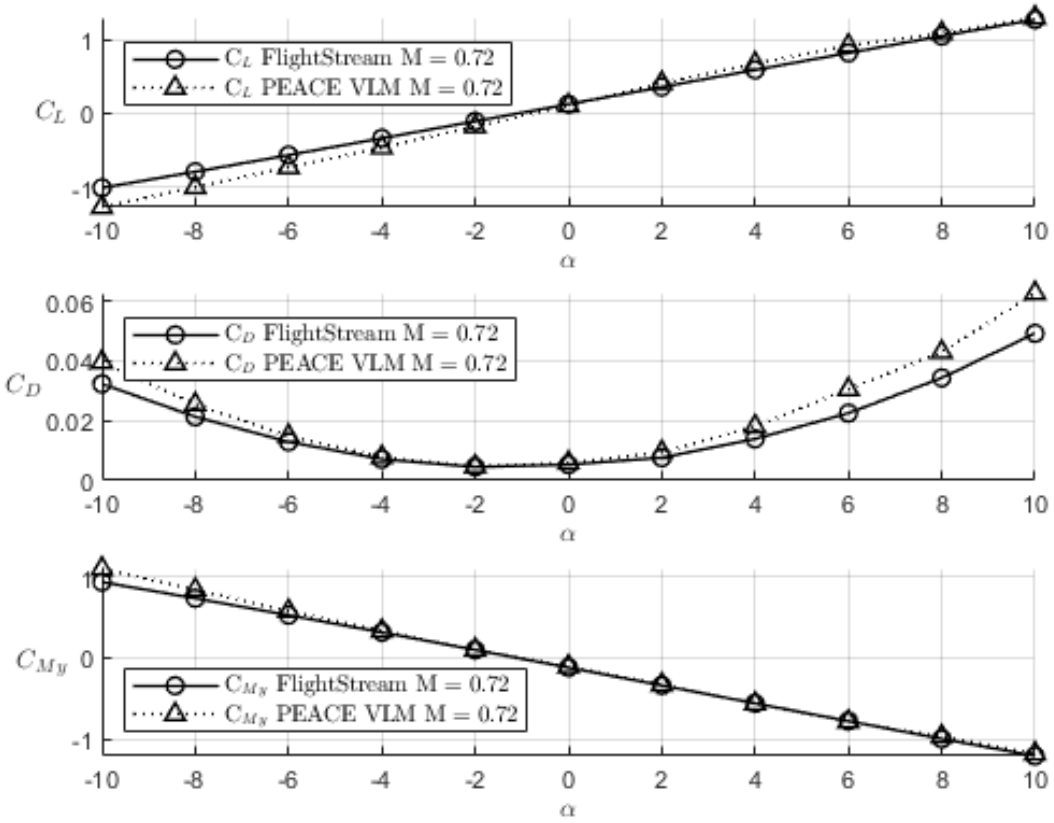

Figure 4.12: A comparison of the results for the full aircraft.

4.3 Variable Geometry Aircraft

As a case study on the modeling of a variable sweep angle wing, a configuration resembling the F-14a was modeled. The F-14 was a fleet defense fighter developed by Northrop Grumman in the late 1960s with its first flight and entry to service in the 1970s. It was employed by the United States Navy to intercept long range bombers far away from the carrier group. The F-14 was designed with the experience gained from the early jets, and it employed a variable sweep angle wing to permit the aircraft to reach high speeds as well as perform slow landings on an aircraft carrier's deck.

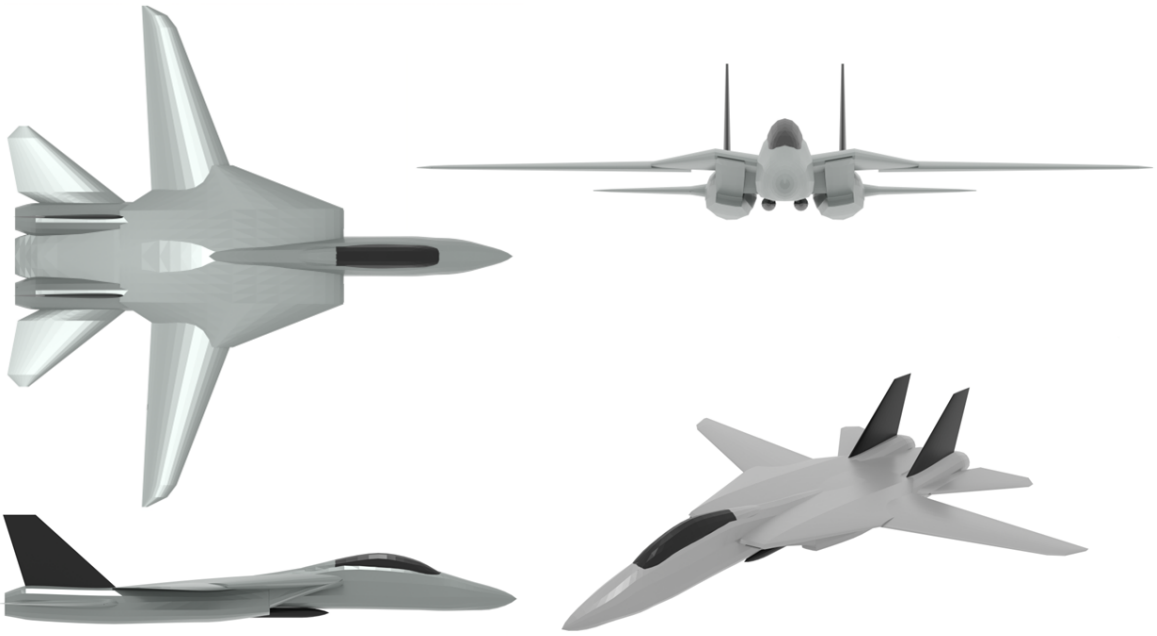

Figure 4.13: Variable geometry aircraft configuration.

Table 4.2: Properties of the variable geometry aircraft.

Property ($\frac{b}{2}$)	**Wing**	**Horizontal Stabilizer**	**Vertical Stabilizer**
Span	7.27 m	3.12 m	2.86 m
Area	16.04m^2	7.75 m^2	6.79 m^2
Taper Ratio	0.38	0.43	0.35
Aspect Ratio	3.3	1.26	1.20
Root Chord	3.44 m	3.28 m	1.26 m
Sweep	20° to 60°	60°	48°

What sets this geometry apart from a conventional aircraft are the options available for the modeling of the variable sweep angle wing. Two solutions were considered:

1. The wing geometry is defined with the known airfoil profiles at a set sweep angle, then the entire wing is rotated about its hinge using a geometry transformation. This method would force the panels to be rotated at an angle relative to the free-stream, but would be the most simple to implement for the geometry processing in the current model. The

relations for the rotation of the wing are given by equation 4.2 where θ is the angle of rotation, P represents the initial coordinates, P' the rotated coordinates, and O is the point about which the rotation is applied. After the rotation is completed for all geometry points, the wake is recomputed using the new trailing edge location. It is essential to apply this rotation before the application of the compressibility corrections to produce a physically correct solution. An illustration of the method is shown in Fig 4.15.

2. The wing geometry is redefined at each sweep angle, and the new airfoil profile is calculated based on the interpolation of points across the wing. This method is harder to implement as it requires the recomputation of individual airfoil data, but it does allow the panels to remain aligned with the direction of the free-stream. An illustration of the airfoil redefinition is shown in Fig. 4.14

$$P' = \begin{bmatrix} \cos\theta & -\sin\theta & 0 \\ \sin\theta & \cos\theta & 0 \\ 0 & 0 & 1 \end{bmatrix} (P - O) \tag{4.2}$$

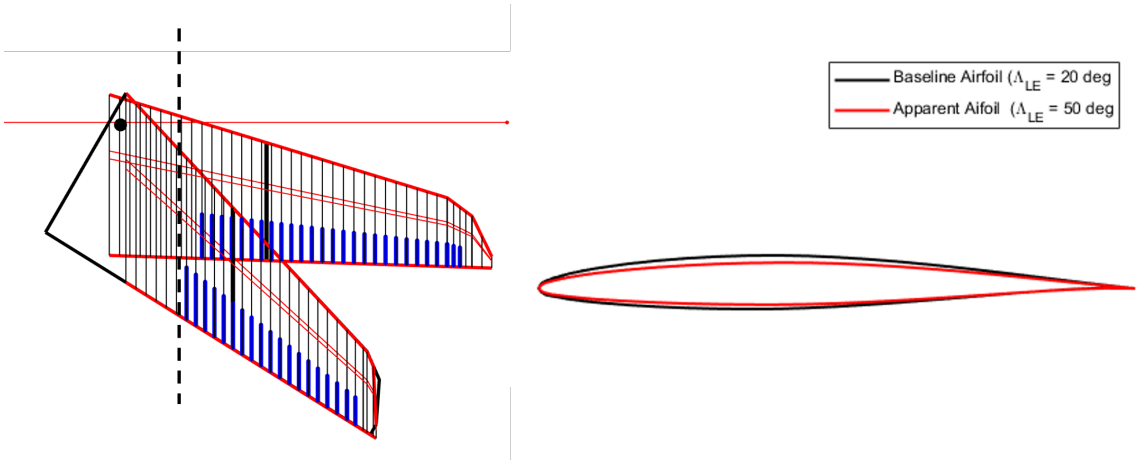

Figure 4.14: The airfoil as seen by the free-stream with varied sweep angles [64].

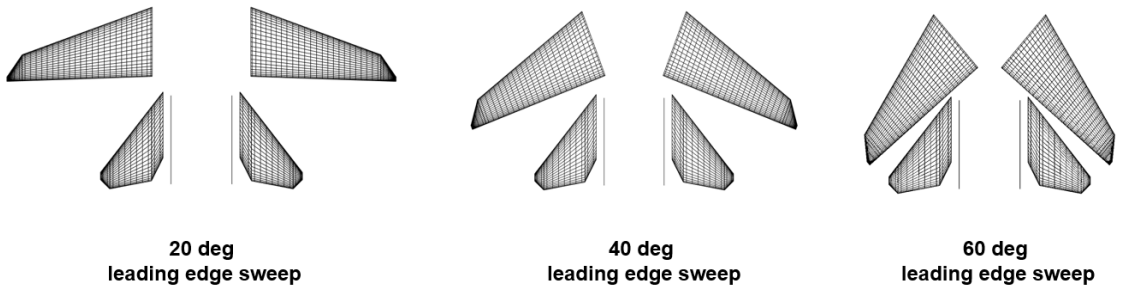

Figure 4.15: The VLM computational mesh at different sweep angles using Method 1 [64].

Since the behavior of the underlying solver is of interest for this test case, the two methods were compared with both OpenVSP and FlightStream. In OpenVSP the wing sweep variations were accomplished by simply rotating the wing about the vertical axis, then repositioning it so that the hinge was in its original position. It therefore follows that the OpenVSP results should approximate the results from Method 1 if all else were equal, however the wake attachment is assumed to be perpendicular to the trailing edge in OpenVSP. The initial few wake vortex segments nearby the wing are not fully aligned with the free stream which is a key differentiator. In addition, the wake relaxation routine employed by OpenVSP further deforms the wake, changing the circulation distribution of the wing. Two cases were run for this experiment, one at mach 0.3 with a leading edge wing sweep of $\Lambda = 20^{\circ}$ and an additional case at mach 0.7 with a sweep of $\Lambda = 60^{\circ}$.

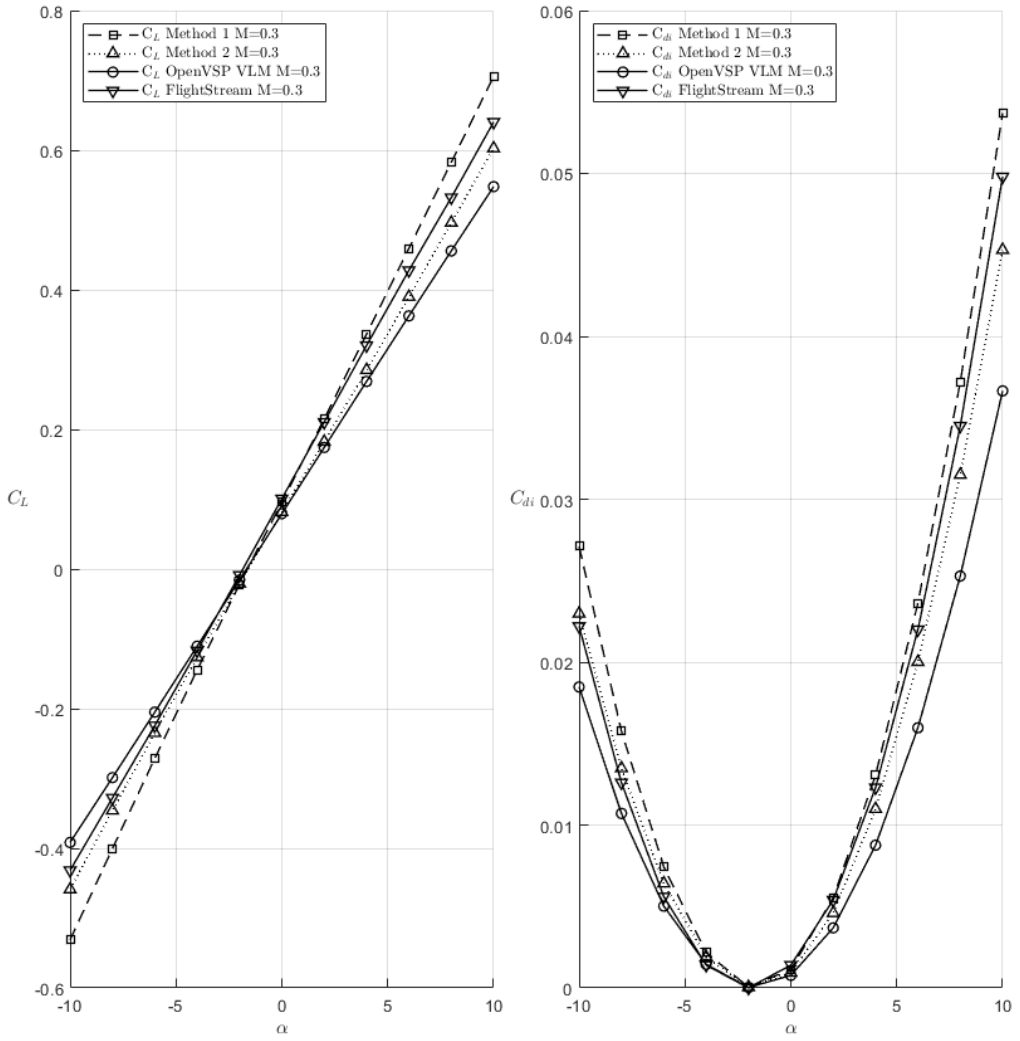

Figure 4.16: The results for mach 0.3 with 20˙ leading edge sweep.

For the case at mach 0.3 with a wing sweep of $\Lambda = 20°$ the results all in agreement. Each method has nearly the same slope, zero lift angle of attack, and the induced drag curves are consistent with the major outliers being OpenVSP and Method 1. The reason that Method 1 does not match Method 2 exactly, even in this unswept condition, is because of the necessary requirement that the wake travel to the trailing edge before deflecting downstream. Figure 4.18 illustrates the paths taken by the wake as it travels downstream.

When the case for mach 0.7 and $\Lambda = 60°$ is considered, there is a clear pattern. Method 2 follows the OpenVSP results closely, and Method 1 is by far the outlier. The FlightStream

results which were generated using the transonic solver, predict a much higher lift curve slope than the other methods. Despite this rise in lift, the induced drag predictions for FlightStream are bounded by Method 1 and 2, with the only outlier for drag calculation being OpenVSP.

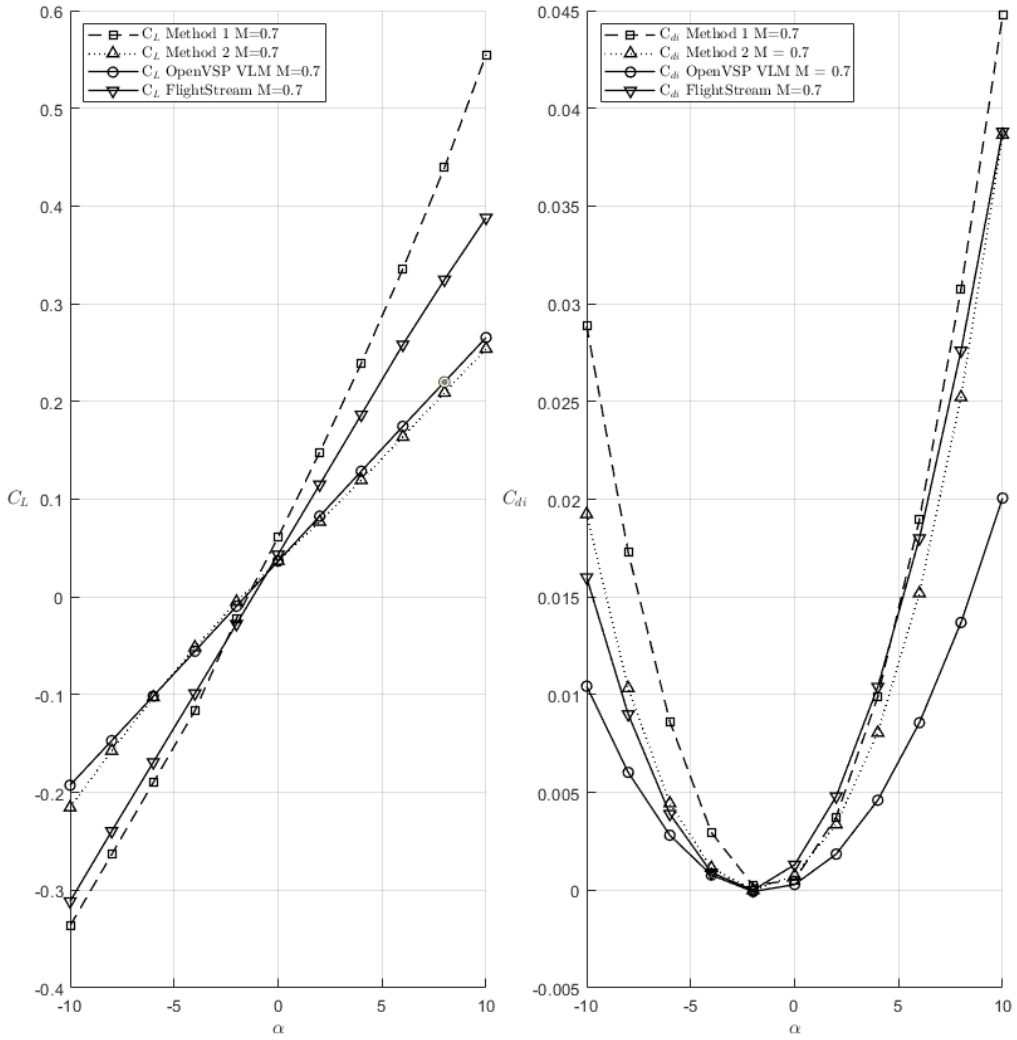

Figure 4.17: The results for mach 0.3 with 20° leading edge sweep.

OpenVSP being an outlier for drag prediction in this case is likely because of the manner in which the solver attaches the wake to the wing. Based on these results, the conclusion is that Method 2 is more accurate than Method 1 in the context of variable sweep wings.

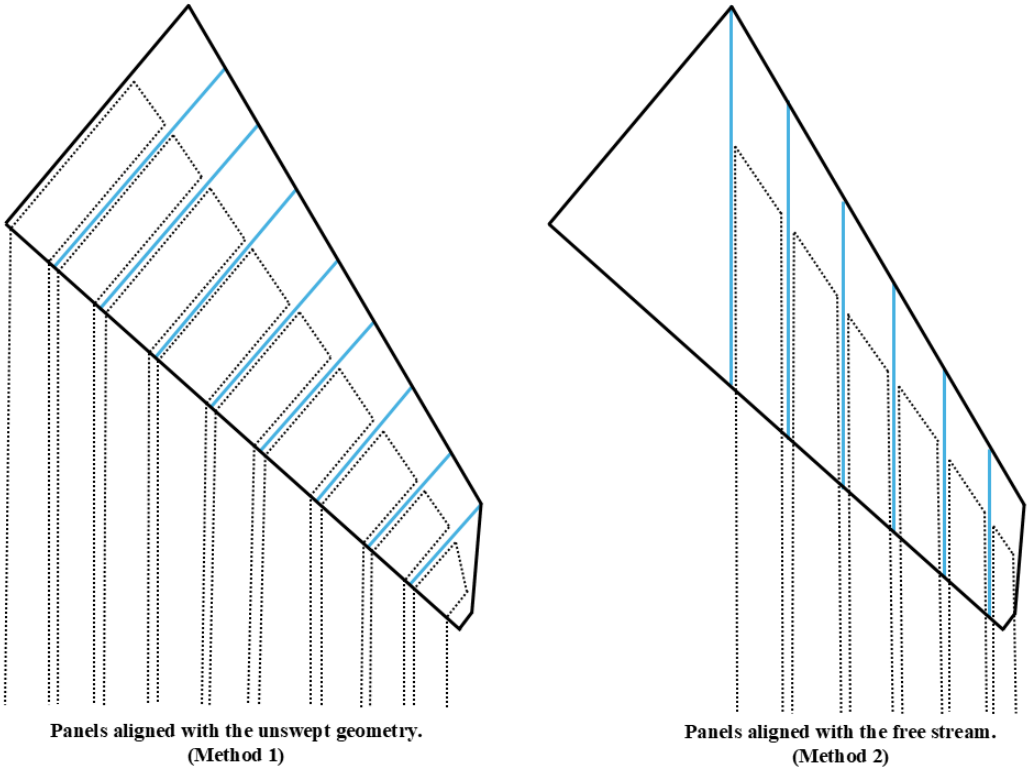

Figure 4.18: The horseshoe vortex arrangement for the two panel definition methods [64].

4.4 Blended Wing Body Aircraft

To demonstrate that the solver is able to handle highly complex wing geometries, a blended wing body (BWB) aircraft was analyzed. This geometry has six distinct airfoil sections with constantly varying incidence, taper, and sweep. The chosen model is NASA's N2A geometry which was based on the SAX-40. The SAX-40 was developed by MIT as an investigation into noise reduction and aerodynamic efficiency of blended wing body aircraft. This design features ultra-high bypass engines with variable nozzles mounted above the wing for noise reduction by providing a physical barrier between the engines and the ground. For increased aerodynamic efficiency, this configuration was designed to produce lift across the entire span of the wing and body section, which allows for a reduction in drag when compared to conventional configurations as the drag from the non-lifting fuselages is completely eliminated. The N2A airframe is featured in numerous works investigating the controllability of BWB configurations and their aerodynamic improvements over traditional aircraft [52, 65–67].

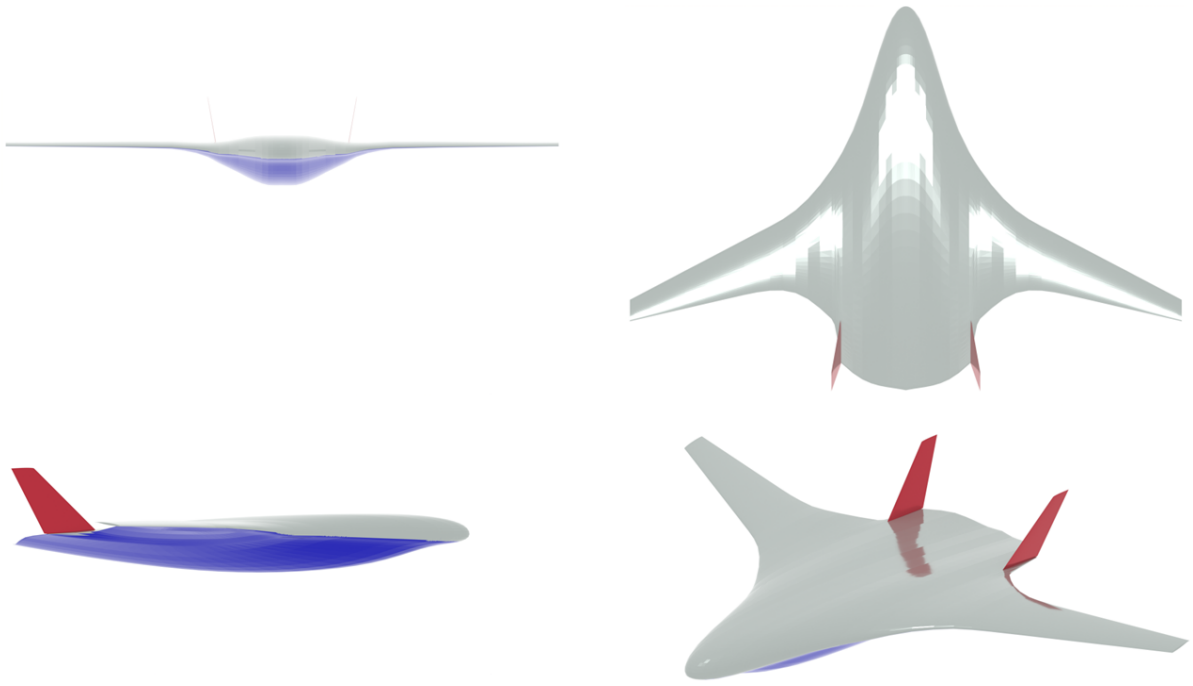

Figure 4.19: The Blended Wing Body aircraft [52].

Unlike the other aircraft configurations presented in this work, the aircraft is entirely composed of thin lifting surfaces the full aircraft can be modeled using VLM without the need to add the contributions of the fuselage. The computational mesh used to generate the results is illustrated in Fig. 4.20.

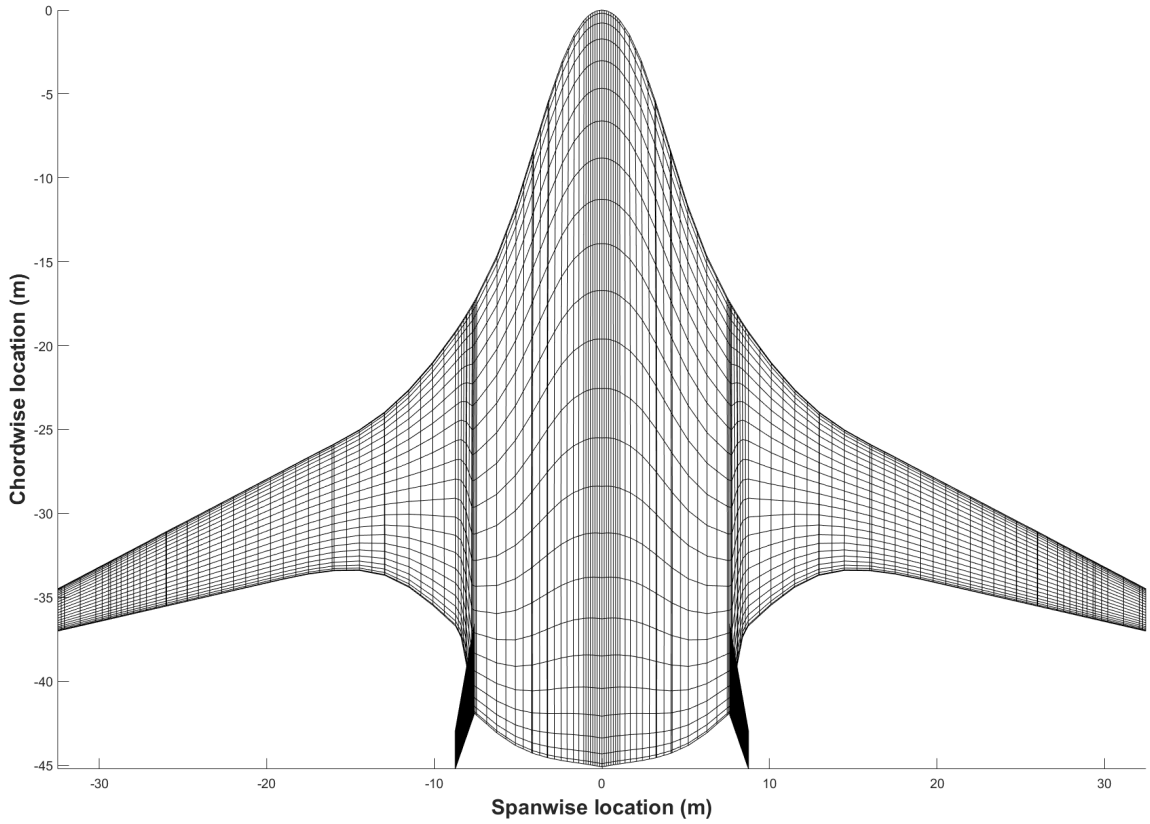

Figure 4.20: The VLM mesh for the blended wing body aircraft.

For comparison, the configuration was evaluated using FlightStream over a sweep of angles of attack for a mach number of 0.2 and 0.78. Both cases assume that the aircraft is shock free. The induced drag was computed from the VLM solution and the total drag was determined using the methods described in Chapter 2. Figure 4.21 provides the spanwise airfoil distribution with η referring to the normalized spanwise location of each airfoil section.

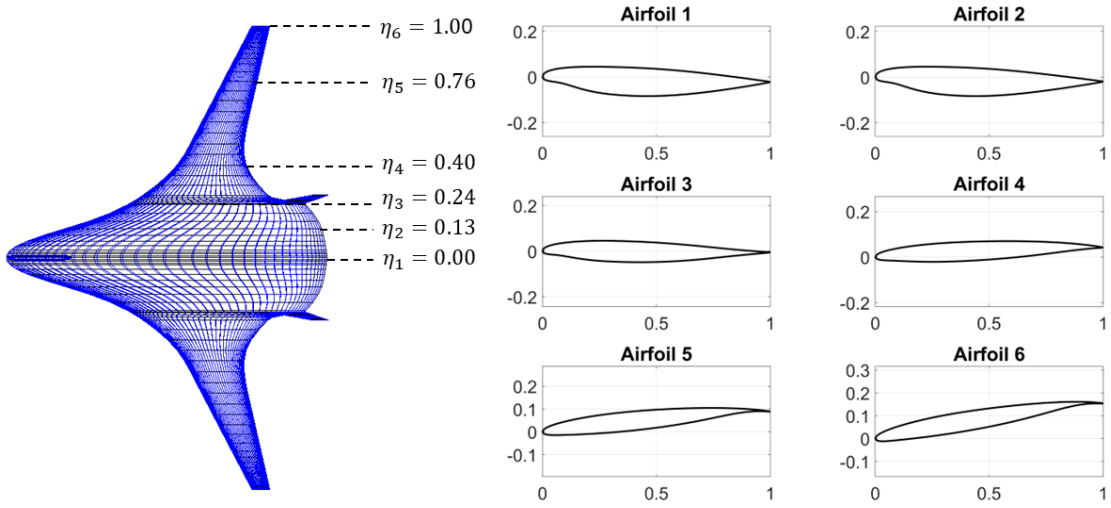

Figure 4.21: The location and identity of airfoil sections on the BWB configurations [52].

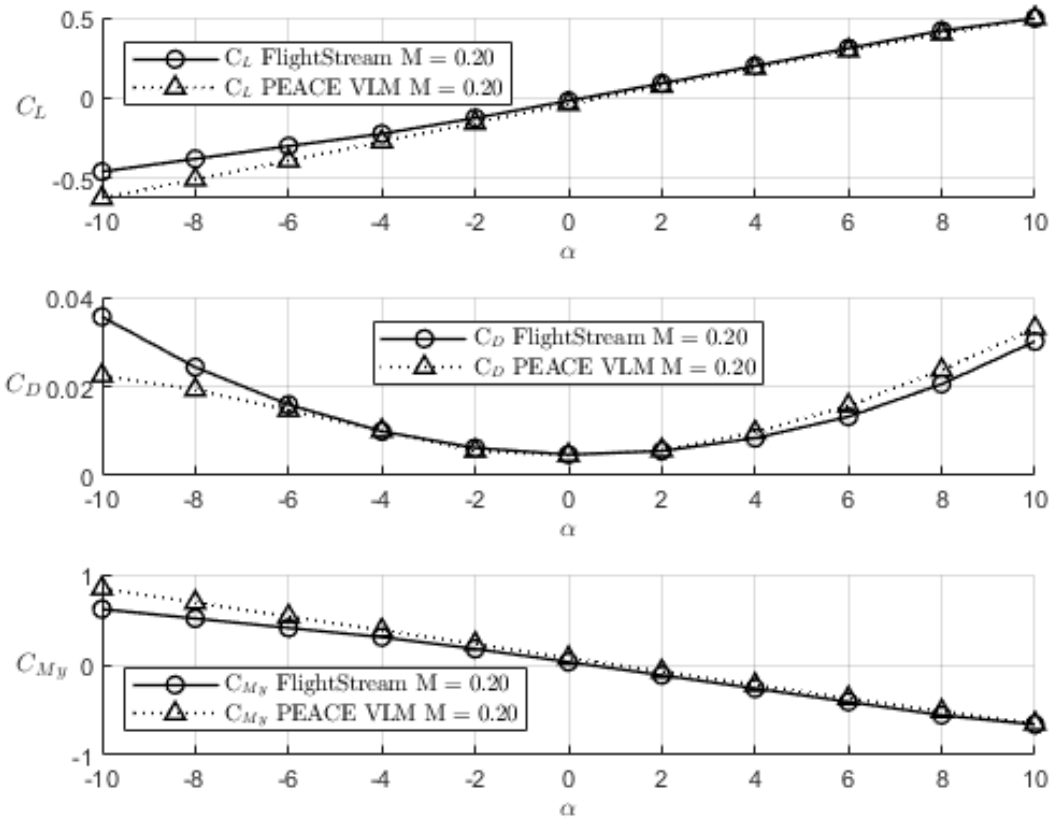

Figure 4.22: The aerodynamic performance for the blended wing body configuration at mach 0.2.

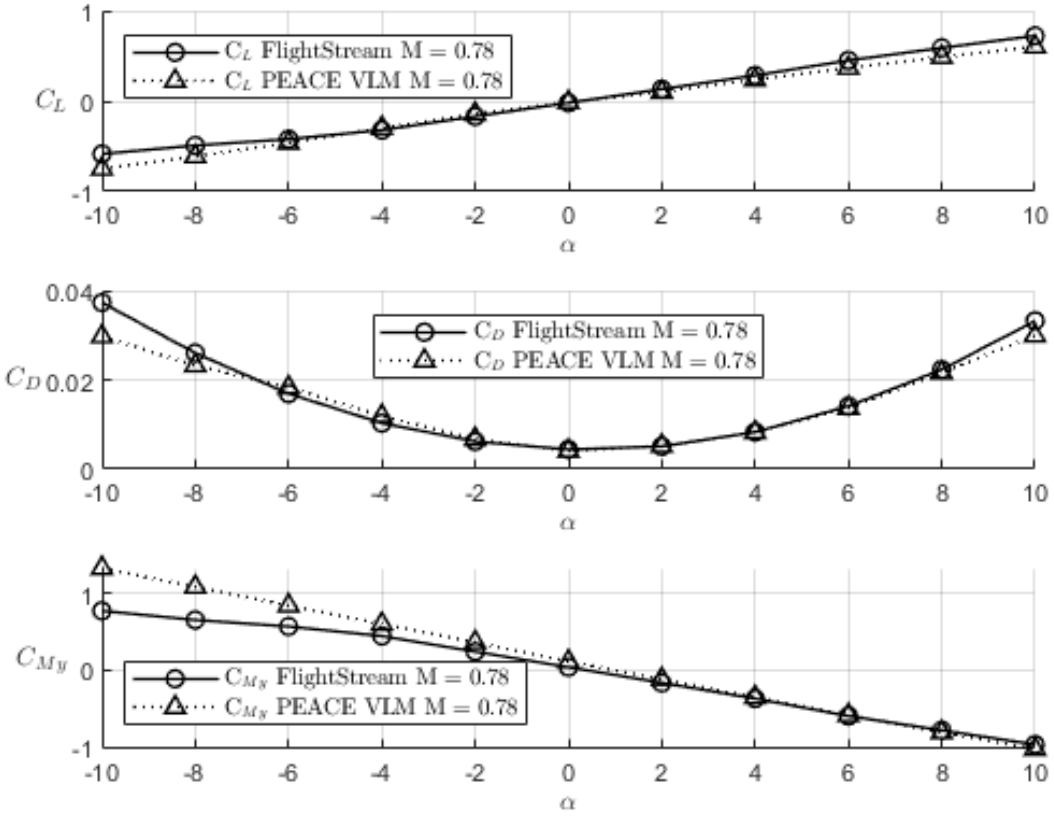

Figure 4.23: The aerodynamic performance for the blended wing body configuration at mach 0.78.

As can be seen in Fig. 4.22 and Fig. 4.23, the present model shows good agreement with FlightStream for small angles of attack. The methods diverge as the angle of attack increases. The performance of the model is consistent across free-stream mach, with the only major change being that the moment coefficient is over-predicted at low speed and under-predicted at high speed. The moment coefficient switching the sign of its error is likely a consequence of the compressibility corrections since scaling the moment coefficient by βPG may cause some configurations to produce larger changes in the moment coefficient than exist in reality.

As the angle of attack approaches negative ten, the models diverge more quickly. This is likely due to the vertical stabilizers interacting with the flow around the rear of the BWB being modeled at a higher fidelity in FlightStream than in the VLM solution. It is of course expected

that the models should diverge at higher angles of attack due to the introduction of non-linear effects in the FlightStream results which are not captured by the VLM solution.

Chapter 5

Conclusion and Future Work

The Vortex Lattice Method provides a way to quickly and accurately predict the aerodynamic loads of lifting surfaces. A VLM aerodynamic solver was developed and integrated into the PEACE sizing framework for aircraft performance analysis. The aerodynamic data generated from the vortex lattice solution was combined with the forces and moments for non-lifting bodies and two-dimensional airfoil data to estimate the flight characteristics of the entire aircraft.

By integrating the solver directly into the framework's aircraft sizing loop, the framework gains the novel ability to determine the performance any lifting surface with no restrictions on the sweep or aspect ratio. In addition, the interactions between the lifting surfaces are directly captured without the need to apply empirical relations.

The results for the base VLM solver were benchmarked with incompressible flow experimental data and found to be in good agreement. Next, the model was evaluated for compressible flow conditions. The model was found to produce results close to FlightStream, which is a higher fidelity Potential Flow solver.

Aerodynamic data from the VLM solver most closely followed the reference data at lower angles of attack, with progressive divergence at higher angles of attack. Behavior like this is to be expected since the formulation of VLM assumes that the object being modeled is a thin lifting surface at a small angle of attack, and the governing equations do not allow for phenomena such as flow separation to be captured without empirical corrections.

A possible avenue for future work is the development of a source and doublet panel solver for non-lifting bodies. If integrated into PEACE, such a solver would be able to generate aerodynamic data for all components of a vehicle without the need for users to generate force

and moment curves in an external software. In addition, the source and doublet solver could be implemented with the VLM solver to compute the cross-influence between non-lifting surfaces and lifting surfaces.

As VLM is currently used in many unsteady flow research codes, another potential option for future work is to extend the model to unsteady flow. By doing this, the model would be able to generate data to tune control systems for disturbance rejection, and PEACE would gain the ability to model flapping wings internally.

The present model does not support supersonic flow conditions, but it is possible to either extend panel methods to capture supersonic flow, or to apply empirical corrections to subsonic flow data to produce similar results. An additional avenue for future work is to extend the VLM solver to capture wave drag and other supersonic flow behaviors.

Bibliography

[1] International Civil Aviation Organization. *Facts and Figures – Economic Development*. https://www.icao.int/sustainability/economic-policy/Pages/Facts-and-Figures.aspx. Accessed: 2025-07-12. 2024.

[2] Aircraft Commerce. "CFM56-5A/5B fuel burn performance". In: *Aircraft Commerce Magazine* 50 (Feb. 2007). Accessed July 14, 2025, p. 13.

[3] Sergi Ros Chaos et al. "Economies of Scale in Cruise Shipping". In: *Maritime Economics & Logistics* 23.4 (2021), pp. 674–696. DOI: 10.1057/s41278-020-00158-3. URL: https://doi.org/10.1057/s41278-020-00158-3.

[4] International Air Transport Association. *Quarterly Air Transport Chartbook Q1 2025*. Accessed: July 14, 2025. 2025. URL: https://www.iata.org/en/iata-repository/publications/economic-reports/quarterly-air-transport-chartbook-q1-2025/.

[5] International Air Transport Association. *Global Outlook for Air Transport: June 2024 Report*. Accessed: July 14, 2025. 2024. URL: https://www.iata.org/en/iata-repository/publications/economic-reports/global-outlook-for-air-transport-june-2024-report/.

[6] Adam P. Johnson. *Weekend Pilots: Technology, Masculinity, and Private Aviation in Postwar America*. Baltimore: Johns Hopkins University Press, 2015.

[7] Wayne Johnson and Christopher Silva. *Observations from Exploration of VTOL Urban Air Mobility Designs*. Presented at a NASA internal meeting or publicly available technical exchange. Oct. 2018.

[8] NASA et al. *Urban Air Mobility (UAM) Market Study*. Market analysis study on UAM applications and outlook. Nov. 2018.

[9] Michael D. Patterson, Kevin R. Antcliff, and Lee W. Kohlman. "A Proposed Approach to Studying Urban Air Mobility Missions Including an Initial Exploration of Mission Requirements". In: *74th Annual Forum & Technology Display, AHS International*. NASA Langley Research Center Technical Paper. American Helicopter Society (AHS) International. Phoenix, Arizona, USA, May 2018.

[10] Yevhenii Kovryzhenko. "Application of the Finite Fourier Series for Smooth Motion Planning of Quadrotors". Master's thesis. MA thesis. Auburn, Alabama: Auburn University, Aug. 2023.

[11] Kaan T. Oner et al. "LQR and SMC Stabilization of a New Unmanned Aerial Vehicle". In: *World Academy of Science, Engineering and Technology* 58 (2009). Sabanci University Unmanned Aerial Vehicle (SUAVI) Project, pp. 674–679.

[12] Liang Gao et al. "Analysis and Control for the Mode Transition of Tandem-Wing Aircraft with Variable Sweep". In: *Aerospace* 9.8 (2022), p. 463.

[13] Na Wang. "A Case Analysis on Amazon Delivery Drones Taking over Traditional Delivery Method". In: *International Journal of Economic Behavior and Organization* 11.1 (2023), pp. 1–6. DOI: 10.11648/j.ijebo.20231101.11. URL: https://doi.org/10.11648/j.ijebo.20231101.11.

[14] Guillaume JJ Ducard and Mike Allenspach. "Review of designs and flight control techniques of hybrid and convertible VTOL UAVs". In: *Aerospace Science and Technology* 118 (2021), p. 107035. DOI: 10.1016/j.ast.2021.107035.

[15] Ferit Cakici and M Kemal Leblebicioglu. "Control System Design of a Vertical Take-off and Landing Fixed-Wing UAV". In: *IFAC-PapersOnLine* 49.3 (2016), pp. 267–272. DOI: 10.1016/j.ifacol.2016.07.965.

[16] Omer Saleem, Muhammad Kazim, and Jamshed Iqbal. “Robust Position Control of VTOL UAVs Using a Linear Quadratic Rate-Varying Integral Tracker: Design and Validation”. In: *Drones* 9.1 (2025), p. 73. DOI: 10.3390/drones9010073.

[17] Shanfei Su et al. “Design and Optimization of a Piecewise Flight Controller for VTOL UAVs”. In: *Journal of Aircraft* 62.1 (2025), pp. 180–197. DOI: 10.2514/1.C037806.

[18] Daniel Raymer. *Aircraft Design: A Conceptual Approach*. 3rd. American Institute of Aeronautics and Astronautics, 2006.

[19] Rajan Bhandari, Aashutosh Aman Mishra, and Imon Chakraborty. “Optimization of Lift-Plus-Cruise Vertical Take-Off and Landing Aircraft with Electrified Propulsion”. In: *Journal of Aircraft* (2024), pp. 1–23.

[20] Stefanus H Putra, Rajan Bhandari, and Imon Chakraborty. “Integrated Vehicle and Subsystems Sizing and Optimization for Advanced Air Mobility Aircraft”. In: *AIAA SCITECH 2024 Forum*. 2024, p. 1085.

[21] Imon Chakraborty et al. “Design and Sizing of an Electrified Lift-Plus-Cruise Ducted Fan Aircraft”. In: *Journal of Aircraft* 60.3 (2023), pp. 817–834.

[22] Imon Chakraborty and Aashutosh Aman Mishra. “Sizing of Tilt-Wing Aircraft with All-Electric and Hybrid-Electric Propulsion”. In: *Journal of Aircraft* 60.1 (2023), pp. 245–264.

[23] Bikash Kunwar et al. “Sizing and Analysis of an Advanced Air Mobility Aircraft Using Parametric Aero-Propulsive Model”. In: *AIAA AVIATION 2023 Forum*. San Diego, CA, 2023.

[24] Jr John D. Anderson. *Fundamentals of Aerodynamics*. 6th. McGraw-Hill Education, 2017.

[25] Joseph Katz and Allen Plotkin. *Low-Speed Aerodynamics*. 2nd. Cambridge University Press, 2001.

[26] Larry L. Erickson. *Panel Methods—An Introduction*. NASA Technical Paper NASA-TM-2995. Moffett Field, California: NASA Ames Research Center, 1990.

[27] Thomas H. Pulliam Harvard Lomax and David W. Zingg. *Fundamentals of Computational Fluid Dynamics*. 2nd. Springer, 1999.

[28] John D. Anderson Jr. *Computational Fluid Dynamics - The Basics with Applications*. 2nd. McGraw-Hill, 1995.

[29] J. A. E. Hasselmann and W. D. V. Riegels. *The Calculation of the Spanwise Load Distribution of Wings by Means of Vortex Lattice Theory*. Tech. rep. R&M 2195. Aeronautical Research Council, 1948.

[30] Paul T. Z. Ting. *Lifting Surface Stability Derivatives by the Vortex Lattice Method*. Tech. rep. NASA TM X-2094. NASA Langley Research Center, 1971.

[31] Ludwig Prandtl. "Tragflügeltheorie". In: *Nachrichten von der Gesellschaft der Wissenschaften zu Göttingen, Mathematisch-Physikalische Klasse* (1918), pp. 451–477.

[32] Charles Hirsch. *Numerical Computation of Internal and External Flows*. 2nd. Vol. 1. John Whiley & Sons, Ltd, 2007.

[33] Mark Drela. *AVL – Athena Vortex Lattice: User Guide and Program Documentation*. `http://web.mit.edu/drela/Public/web/avl/`. Massachusetts Institute of Technology, Department of Aeronautics and Astronautics. 2025.

[34] NASA OpenVSP Development Team. *OpenVSP User Manual*. `https://openvsp.org/wiki/doku.php?id=start`. NASA Langley Research Center. 2025.

[35] Tomas Melin. "A Vortex Lattice MATLAB Implementation for Linear Aerodynamic Wing Applications". Includes the original Tornado User Guide. MA thesis. Royal Institute of Technology (KTH), Stockholm, Sweden, 2000.

[36] Tomas Melin. *Tornado 1.0 User's Guide: Reference Manual for the Tornado Vortex Lattice Method*. Royal Institute of Technology (KTH). 2001. URL: `https://www.researchgate.net/publication/320924935_Tornado_10_USER%27s_GUIDE_Reference_manual`.

[37] Harshavardhan Joshi and Pierre Thomas. “Unsteady Vortex Lattice Method in Tornado: A Fast and Cost-Effective Solver for Dynamic Analysis of Supersonic Lifting Surfaces”. In: *Aerospace Europe Conference 2023*. EUROAVIA / EUCASS. 2023. URL: https://www.eucass.eu/doi/EUCASS2023-092.pdf.

[38] Mathieu Parenteau and Éric Laurendeau. “Nonlinear Frequency-Domain Solver for Vortex Lattice Method”. In: *AIAA Journal* 56.6 (June 2018). DOI: 10.2514/1.J056704.

[39] Vincent Proulx-Cabana et al. “A Hybrid Non-Linear Unsteady Vortex Lattice-Vortex Particle Method for Rotor Blades Aerodynamic Simulations”. In: *Fluids* 7.2 (2022), p. 81. DOI: 10.3390/fluids7020081.

[40] S. A. Dovgii and A. V. Shekhovtsov. “An Improved Vortex Lattice Method for Nonstationary Problems”. In: *Journal of Mathematical Sciences* 104.6 (2001). Translated from Obchyslyuval’na ta Prykladna Matematka, No. 82, 1997, pp. 30–44, pp. 1615–1629. DOI: 10.1023/A:1010470609470.

[41] Bret K. Stanford and Philip S. Beran. “Analytical Sensitivity Analysis of an Unsteady Vortex-Lattice Method for Flapping-Wing Optimization”. In: *Journal of Aircraft* 47.2 (2010). Presented as Paper 2614 at the AIAA Structures, Structural Dynamics, and Materials Conference, Palm Springs, CA, 4–7 May 2009, pp. 647–656. DOI: 10.2514/1.46259.

[42] Robert J. S. Simpson, Rafael Palacios, and Joseba Murua. “Induced-Drag Calculations in the Unsteady Vortex Lattice Method”. In: *AIAA Journal* 51.7 (July 2013). Technical Notes, pp. 1775–1779. DOI: 10.2514/1.J052136.

[43] Mario Lee and Chih-Ming Ho. “Lift force of delta wings”. In: *Applied Mechanics Reviews* 43.9 (1990), pp. 209–221. DOI: 10.1115/1.3119501.

[44] P. Konstadinopoulos et al. “A Vortex-Lattice Method for General, Unsteady Aerodynamics”. In: *Journal of Aircraft* 22.1 (Jan. 1985), pp. 38–44.

[45] Timothy T. Takahashi and Che-Wei Ou. “When Higher Fidelity Models Degrade Our Understanding of Induced Drag – The Tragedy of the Trefftz Plane Integral”. In: *AIAA*

Scitech 2020 Forum. Orlando, FL: American Institute of Aeronautics and Astronautics, Jan. 2020. DOI: 10.2514/6.2020-0276.

[46] Anh Tuan Nguyen et al. "Extended Unsteady Vortex-Lattice Method for Insect Flapping Wings". In: *Journal of Aircraft* 53.6 (2016). DOI: 10.2514/1.C033456.

[47] Youcef Saad and Martin H. Schultz. "GMRES: A generalized minimal residual algorithm for solving nonsymmetric linear systems". In: *SIAM Journal on Scientific and Statistical Computing* 7.3 (1986), pp. 856–869.

[48] Santiago Pinzón. "Introduction to Vortex Lattice Theory". In: *Ciencia y Poder Aéreo* 10 (2015). ISSN 1909-7050 / E-ISSN 2389-2468. Received: 30/09/2015. Approved by internal evaluator: 06/11/2015. Approved by external evaluator: 27/11/2015, pp. 1–260. URL: http://dx.doi.org/10.18667/cienciaypoderaereo.433.

[49] I Chakraborty and A.A. Mishra. "A Generalized Energy-based Flight Vehicle Sizing and Performance Analysis Methodology". In: *Journal of Aircraft* 58.4 (2021), pp. 762–780.

[50] I Chakraborty and A.A. Mishra. "Sizing and ANalysis of a Lift-Plus-Cruise Aircraft with Electrified Propulsion". In: *Journal of Aircraft* 60.3 (2023), pp. 747–765.

[51] I Chakraborty et al. "Design and Sizing of an Electrified Lift-Plus-Cruise Ducted Fan Aircraft". In: *Journal of Aircraft* 60.3 (2023), pp. 817–834.

[52] B. Davis et al. "Multi-Objective Design Optimization of a Liquid Hydrogen Blended Wing Body Aircraft Concept". In: *AIAA AVIATION 2025 Forum*. AIAA-2025-2070. Las Vegas, Nevada, 2025.

[53] Andrew B. Lambe and Joaquim R. R. A. Martins. "Extensions to the Design Structure Matrix for the Description of Multidisciplinary Design, Analysis, and Optimization Processes". In: *Structural and Multidisciplinary Optimization* 46 (2012), pp. 273–284. DOI: 10.1007/s00158-012-0763-y.

[54] Aashutosh Aman Mishra, Rajan Bhandari, and Imon Chakraborty. "Sizing and Analysis of Hybrid-Electric Single Main Rotor NOTAR Helicopters using the PEACE Framework". In: *AIAA AVIATION 2025 Forum*. Las Vegas, NV, 2025.

[55] Bikash Kunwar et al. “Sizing and Optimization of an Urban Air Mobility Aircraft Using Parametric Aero-Propulsive Model”. In: *AIAA AVIATION 2023 Forum*. 2023, p. 3662.

[56] R. Bhandari and I. Chakraborty. “Genetic Algorithm Optimization of Lift-Plus-Cruise VTOL Aircraft with Electrified Propulsion”. In: *AIAA SCITECH 2023 Forum*. National Harbor, MD: AIAA-2023-xxxx, Jan. 2023, p. 1.

[57] RD Finck. *USAF (United States Air Force) Stability and Control DATCOM (Data Compendium)*. Tech. rep. MCDONNELL AIRCRAFT CO ST LOUIS MO, 1978.

[58] John Deyoung. *Theoretical antisymmetric span loading for wings of arbitrary plan form at subsonic speeds*. NTRS Author Affiliations: NTRS Report/Patent Number: NACA-TR-1056 NTRS Document ID: 19930092101 NTRS Research Center: Legacy CDMS (CDMS). Jan. 1951. URL: https://ntrs.nasa.gov/citations/19930092101 (visited on 06/13/2024).

[59] J. Weber, D. Küchemann, and G. G. Brebner. *Low-Speed Tests on 45-Degree Swept-Back Wings, Parts I and II*. Reports and Memoranda 2882. Crown Copyright Reserved. London: Aeronautical Research Council, Ministry of Supply, May 1958.

[60] Boeing. *First Boeing Next-Generation 737-800 Goes To Hapag-Lloyd*. https://www.boeing.com/news/releases/1998/news_release_1998_0423a.html. Press release, April 23, 1998. Archived from the original on September 15, 2020. Retrieved September 5, 2020. 1998.

[61] Alex Derber. “Inside MRO: Boeing 737-800 Not Expected To Peak Until 2021”. In: *MRO Network, Aviation Week & Space Technology* (June 2018). Archived from the original on August 18, 2018. Retrieved August 17, 2018. URL: https://www.mro-network.com/maintenance-repair-overhaul/inside-mro-boeing-737-800-not-expected-peak-until-2021.

[62] James L. Thomas. *Subsonic finite elements for wing-body combinations*. NASA Technical Memorandum N76-28165. NASA TM-X-72636. NASA Langley Research Center, 1976.

[63] H. N. V. Dutt and S. R. Rajeswari. “Wing-body interference using a hybrid panel method”. In: *Acta Mechanica* 106 (1994), pp. 111–126.

[64] B. Kunwar et al. “Integrating Strip-Theory Aerodynamics into Conceptual Design of Variable Geometry Swing-Wing Aircraft”. In: *AIAA AVIATION 2025 Forum*. AIAA-2025-2070. Las Vegas, Nevada, 2025.

[65] Gregory M. Gatlin, Dan D. Vicroy, and Melissa B. Carter. *Experimental Investigation of the Low-Speed Aerodynamic Characteristics of a 5.8-Percent Scale Hybrid Wing Body Configuration*. Tech. rep. NASA/TM–2012-217652. American Institute of Aeronautics and Astronautics. Hampton, VA: NASA Langley Research Center, 2012.

[66] Stephanie L. Heath et al. *NASA Hybrid Wing Aircraft Aeroacoustic Test Documentation Report*. Tech. rep. NASA/TM–2016-219185. Hampton, VA: NASA, 2016.

[67] Michael T. Tong et al. *Engine Conceptual Design Studies for a Hybrid Wing Body Aircraft*. Tech. rep. NASA/TM–2009-215680, ARL–TR–4719, GT2009–59568. Cleveland, OH: NASA Glenn Research Center and U.S. Army Research Laboratory, 2009.